1 **MESSENGER Observations of Disappearing Dayside Magnetosphere Events**

2 **at Mercury**

3

4 **J. A. Slavin[1], H. R. Middleton[2], J. M. Raines[1], Xianzhe Jia[1], J. Zhong[3], W. -J. Sun[1], S.**

5 **Livi[1,4], S. M. Imber[1,5], G. -K. Poh[1,6], M. Akavan-Tafti[1], J. Jasinski[1,7], G. A. DiBraccio[6], C.**

6 **Dong[8], R. M. Dewey[1], and M. L. Mays[6]**

7 [1]University of Michigan, Ann Arbor, MI 48109.

8 [2]ESA European Space and Astronomy Center, Madrid, Spain

9 [3]Key Laboratory of Earth and Planetary Physics, Chinese Academy of Sciences,

10 Beijing, China

11 [4]Southwest Research Institute, San Antonio, Texas

12 [5]University of Leicester, Leicester, United Kingdom

13 [6]NASA Goddard Space Flight Center, Greenbelt, MD

14 [7]Jet Propulsion Laboratory, California Institute of Technology, Pasadena, CA

15 [8]Princeton Plasma Physics Laboratory, Princeton Univ., Princeton, NJ

16

17 Corresponding author: James A. Slavin (jaslavin@umich.edu)

1

20

21   **Key Points:**

22   • The dayside magnetosphere of Mercury is observed to disappear at MESSENGER's orbit

23   during some coronal mass ejection impacts

24   • The cause appears to be extreme solar wind compression and/or reconnection-driven

25   erosion of Mercury's dayside magnetic field

26   • The low altitude of the bow shock during these events strongly suggests that Mercury's

27   dayside surface experiences direct solar wind impact

28

2

29 **Abstract**

30 MESSENGER measurements taken during passes over Mercury's dayside hemisphere indicate

31 that on 4 occasions the spacecraft remained in the magnetosheath even though it reached

32 altitudes below 300 km. During these disappearing dayside magnetosphere (DDM) events,

33 MESSENGER did not encounter the magnetopause until it was at very high magnetic latitudes, ~

34 66 to 80°. These DDM events stand-out with respect to their extremely high solar wind dynamic

35 pressures, P_{sw} ~ 140 to 290 nPa, and intense southward magnetic fields, B_z ~ - 100 to - 400 nT,

36 measured in the magnetosheath. In addition, the bow shock was observed very close to the

37 surface during these events with a subsolar altitude of ~ 1200 km. It is suggested that DDM

38 events, which are closely associated with coronal mass ejections, are due to solar wind

39 compression and/or reconnection-driven erosion of the dayside magnetosphere. The very low

40 altitude of the bow shock during these events strongly suggests that the solar wind impacts much

41 of Mercury's sunlit hemisphere during these events. More study of these disappearing dayside

42 events is required, but it is likely that solar wind sputtering of neutrals from the surface into the

43 exosphere maximizes during these intervals.

44

45 **1.0 Introduction**

46   Since the initial Mariner 10 discovery of it's weak, rotation-axis-aligned dipolar magnetic

47 field [Ness et al., 1974; Anderson et al., 2011], there has been great interest in this, the smallest

48 of the Solar System's six planetary magnetospheres. The mean distance from the internal dipole

49 to the nose of Mercury's magnetopause is only ~ 1.5 R_M [Slavin et al., 2009; Winslow et al.,

50 2013; Zhong et al., 2015a]. As originally found by Mariner 10, the structure of Mercury's

3

51   magnetosphere is quite similar in many ways to that of the Earth [e.g. Alexeev et al, 2010; Slavin

52   et al., 2012]. However, the features of the Earth's magnetosphere that map to the interior of

53   Mercury due to its large size relative to its magnetosphere, such as a radiation belts and Region 2

54   currents, are not present [Ogilvie et al., 1976; Slavin et al., 1997]. Mercury's magnetic dipole is

55   offset to the north by 0.2 R_M (1 R_M = 2440 km) [Alexeev et al., 2010; Anderson et al., 2011],

56   which introduces significant north/south asymmetries in the polar magnetic fields, the size of the

57   polar caps, the loss cones and other phenomena [see review by Korth et al., 2019]. Numerical

58   simulations of the solar wind interaction with Mercury's magnetic field have reproduced much

59   of the magnetospheric structure observed by Mariner 10 and MESSENGER [Kabin et al., 2000;

60   Janhunen and Kallio, 2004; Kidder et al., 2008; Trávníček et al., 2009, 2010; Benna et al., 2010;

61   Wang et al., 2010; Mueller et al., 2012; Varela et al., 2015; Jia et al., 2015; Dong et al., 2019].

62   Despite the small dimensions of Mercury's dayside magnetosphere and the high solar

63   wind pressure in the inner Solar System, numerous studies have found that simple Earth-like

64   compression of the forward magnetopause will place the magnetopause within a few proton

65   gyroradii (where 1 gyroradius ~ 50 km for solar wind protons) no more than a few per cent of the

66   time [e.g., Siscoe and Christopher, 1975; Slavin et al., 1979; Winslow et al., 2013; Zhong et al.,

67   2015b; Johnson et al., 2016]. This conclusion was bolstered by the work of Hood and Schubert

68   (1979) and Suess and Goldstein (1979) who first modeled the effects of induction currents driven

69   within Mercury's interior by solar wind pressure enhancements.

70   These currents are expected to flow on the surface of Mercury's ~ 2000 km radius iron

71   core [Smith et al., 2012] as shown in Figure 1a [from Slavin et al., 2014]. Their results indicated

72   that induction would "stiffen" the planetary magnetic field to the point where solar wind ram

73   pressures of ~ 200 to 250 nPa would be required to compress the magnetopause to the surface.

4

74 The cause of this stiffening are induction currents driven on the surface of the iron core

75 [Glassmeier et al., 2009] which, when added to the deep dynamo currents, changes Mercury's

76 total magnetic moment [Slavin et al., 2014; Jia et al., 2019; Dong et al., 2019]. In response to

77 compression (rarefaction) of the planetary magnetic field the induction currents act to increase

78 (decrease) the total magnetic moment.

79   Figure 1a depicts this effect by coloring the closed dipolar magnetic fields in the dayside

80 magnetosphere according to their source. The dipolar magnetic fields due to the core dynamo are

81 yellow while the magnetic fields due to induction are green. Slavin et al. (2014) first

82 demonstrated the effects of these induction currents on the stand-off distance of the

83 magnetopause using MESSENGER data collected during coronal mass ejections (CMEs) and

84 high-speed streams (HSSs). These interplanetary events typically bring with them sudden solar

85 wind pressure increases of ~ 3 to 5 times the mean observed at Mercury. The effects of more

86 modest changes in the solar wind pressure on induction currents as Mercury moves between its

87 perihelion and aphelion have been well modeled by Zhong et al. (2015b) and Johnson et al.

88 (2016).

89   Reconnection at the dayside magnetopause transfers magnetic flux from the closed-field-

90 line region in the forward magnetosphere into the open-field-line lobe regions of the magnetotail

91 as illustrated in Figure 1b. The return circulation is driven by reconnection in the cross-tail

92 current sheet. The complete circulation of magnetic flux and plasma to the tail and back again is

93 termed the "Dungey cycle" [Dungey, 1961]. The speed of the internal plasma convection and

94 the scale of the system determine the length of the Dungey cycle, which is 1 – 3 hrs at Earth

95 [e.g., Borovsky et al., 1993; Tanskanen et al., 2009]. At Mercury, however, the time required for

96 this cycle is only ~ 3 minutes [Siscoe et al., 1975; Slavin et al., 2010a; Imber and Slavin, 2017].

5

97 For this reason, Mercury's magnetosphere can move from quiescent to disturbed states on time

98 scales of only a few minutes. This is much faster than the 30 – 60 min that MESSENGER spent

99 inside Mercury's magnetosphere each orbit [see Slavin et al., 2019].

100 At Earth a large magnetic shear, greater than 90°, across the magnetopause is generally

101 necessary before intense magnetic reconnection can occur [Paschmann et al., 1986; Sonnerup et

102 al., 1990; Webster et al., 2018]. These larger shears are present whenever the upstream IMF has

103 a southward component and they increase as B_z becomes increasingly negative. Mercury's

104 response to IMF has been found to be somewhat different with the effects of reconnection

105 usually being present whenever there is even small magnetic shear across the magnetopause

106 [Slavin et al., 2009; DiBraccio et al., 2013]. Gershman et al. (2013) examined the intense draped

107 magnetic fields in the dayside magnetosheath and argued that they are due to the low solar wind

108 Alfvenic Mach number (M_A) conditions in the inner Solar System. They found, in agreement

109 with the theoretical arguments of Zwan and Wolf (1976), that the MESSENGER observations

110 were consistent with the low solar wind M_A reducing the plasma heating at the bow shock and

111 producing a low-β magnetosheath, where β is the ratio of plasma thermal pressure to magnetic

112 pressure. Under these conditions, the stress exerted on the subsolar magnetosheath by the solar

113 wind is increasingly supported by the draped IMF. This, and the weak plasma heating at the low

114 Mach number bow shock, contributes to the formation of the thick, low-β plasma depletion layer

115 (PDL) adjacent to the magnetopause that is unique Mercury's interaction with the solar wind

116 [Zwan and Wolf, 1976; Gershman et al., 2013].

117 An important aspect of the thick PDL at Mercury is that magnetopause reconnection

118 usually involves magnetic fields that are comparable in magnitude on both sides of the current

119 sheet, a situation that is termed "symmetric" reconnection. In contrast "asymmetric"

6

120 reconnection is the typical for the magnetopause boundary at all of the other intrinsic

121 magnetospheres because they are located farther from the Sun where the solar wind M_A is much

122 higher. This is an important distinction because, for comparable magnetic shear angles,

123 symmetric reconnection is always faster than the asymmetric case due to the high Alfven speed

124 on both sides of the reconnecting current sheet [e.g. Sonnerup, 1974]. In fact, Slavin and Holzer

125 (1979) argued that, on average, the rate of reconnection at Mercury would be found to be greater

126 than at Earth due to the high Alfvénic speed and low M_A conditions in the inner Solar System.

127 Further, they used the observed effects of reconnection at Earth and scaling arguments to predict

128 that the magnetopause at Mercury would often be eroded to very low altitudes where solar wind

129 impact could take place. However, the impact of induction in the interior of the planet was not

130 considered in this early analysis.

131 Dayside reconnection at Mercury has broad impacts on this planet's environment because

132 of the role of solar wind precipitation on surface sputtering and volatile desorption into its

133 neutral exosphere [Killen et al., 2019] and the transfer of solar wind energy and plasma into this

134 small, but extremely dynamic magnetosphere [Slavin et al., 2019]. The newly opened Mercury

135 field lines carried tailward by the solar wind all map to the north or south magnetospheric cusps

136 and pivot about the cusps as the high-altitude end is incorporated into the tail lobes. These tail

137 magnetic fields that have recently been added to the outer layers of the tail lobes then convect

138 equatorward toward the cross-tail current sheet. Solar wind particles generally have a significant

139 component of their velocity parallel to the interplanetary magnetic field. Following reconnection

140 between the IMF and the planetary magnetic field, many of these solar wind particles are

141 channeled inward toward the planetary surface where they will impact unless mirroring takes

142 place first [Raines et al., 2014; Jasinski et al., 2017]. Particles within magnetic flux tubes known

143 as cusp plasma filaments [Slavin et al., 2014]. Detailed analyses by Poh et al. (2016) have shown

144 that it is very likely that these filaments are the low altitude extensions of flux transfer events.

145 They have been shown to magnetically map down to the surface foot print of the cusp where

146 they contribute significantly to particle precipitation in Mercury's cusp region [Poh et al., 2016].

147 For these reasons, Mercury's magnetospheric cusp is believed to be primary sites for solar wind

148 impact on Mercury's surface with the southern cusp being larger in area due to the northward

149 offset of the planetary dipole [Massetti et al., 2003; Sarantos et al., 2007] with the southern cusp

150 being the larger of the two due to the northern offset of the cusp [Korth et al., 2019]. The direct

151 impact of solar wind protons not only sputters neutral atoms into Mercury's exosphere [e.g.,

152 Pfleger et al., 2015], but it also sputters ions into the high-latitude magnetotail where they mix

153 with solar wind that mirrored at low altitudes to form the plasma mantle [DiBraccio et al., 2015;

154 Jasinski et al., 2017]. This impact of solar wind plasma beneath the cusps also contributes to

155 space weathering of the surface [Domingue et al., 2014; Pfleger et al., 2015].

156   In this study, we examine 4 low-altitude MESSENGER passes over the dayside

157 hemisphere of Mercury for which *no dayside magnetosphere, only magnetosheath plasma was*

158 *observed*. Such events, or ones similar to them, have been noted previously by Raines et al.

159 (2015), Zhong et al. (2015a), Slavin et al. (2019) and Winslow et al. (2019), but not analyzed in

160 detail beyond noting their presence in the MESSENGER data set. We term these intervals

161 "disappearing dayside magnetosphere" (DDM) events. On these occasions magnetosheath

162 plasma was observed as MESSENGER moved either poleward (3 cases) or equatorward (1 case)

163 over the dayside hemisphere of Mercury with the magnetosphere not being entered and the

164 magnetopause not being crossed until the spacecraft was at very high-latitudes just forward of

165 the terminator plane [Raines et al., 2014; Zong et al., 2015a; Slavin et al., 2019]. Here we will

8

166 show that the DDM intervals stand-out with respect to their extremely high solar wind pressures,

167 ~ 140 to 290 nPa, which were inferred from the analysis of the high-latitude magnetopause

168 crossings. These very high solar wind pressures were supported by CCMC ENLIL-WSA + Cone

169 model runs based upon CME observations by other spacecraft. We also find that intense

170 southward magnetic fields, B_z ~ - 100 to - 400 nT are present in the magnetosheath and very high

171 frequent encounters with flux transfer events (FTEs) are recorded by MESSENGER with the

172 peak frequency occurring over the northern cusp. During these DDM events the forward bow

173 shock was also observed to be located unusually close to the planet, ~ 1200 km, or slightly less

174 than half of its mean altitude. It is suggested that these DDM events, which are all associated

175 with CME impacts, are due to extreme solar wind compression and/or reconnection-driven

176 erosion of the dayside magnetosphere. It is likely that the solar wind directly interacts with the

177 surface over much of Mercury's sunlit hemisphere during DDM intervals. For this reason it is

178 likely that the maximum contribution of solar wind surface sputtering to Mercury's neutral

179 exosphere takes place during these events.

180

181 **2.0 MESSENGER Mission**

182 The MErcury Surface, Space ENvironment, GEochemistry, and Ranging (MESSENGER)

183 spacecraft was inserted into a ~ 12 h period, 82° inclination, high eccentricity (~200 × 15,000 km

184 altitude) orbit about Mercury on 18 March 2011 [Solomon et al., 2007]. The period of the orbit

185 was reduced on 16 April 2012 to ~ 8 hr by lowering the apoapsis altitude to ~10,000 km. This

186 change in apoapsis part way through the mission resulted in rather complete sampling of

187 Mercury's magnetosphere and its principal current layers from the nose region and ~ 3 to 4 R_M

188 downstream of the center of the planet. The trajectory of the spacecraft over its ~ 4 years in orbit

9

189   is plotted in Figure 2. Average bow shock and magnetopause surfaces [Winslow et al., 2013] are

190   shown for comparison. The coordinates utilized are solar wind aberrated cylindrical Mercury

191   Solar Orbital (MSO) coordinates wherein the X_{MSO} axis points from Mercury's center toward the

192   Sun, the Y_{MSO} axis lies in Mercury's orbital plane about the Sun and it is positive in the direction

193   opposite to planetary motion and Z_{MSO} completes the right-handed orthogonal system. The solar

194   wind aberration is indicated by the primes, X'_{MSO}, Y'_{MSO} and Z'_{MSO}. The aberration has been

195   carried out using Mercury's azimuthal speed about the Sun and rotating the MSO X and Y axes

196   until X'_{MSO} is opposite to an assumed mean 400 km/s radial solar wind. After depleting the last

197   of its fuel, the MESSENGER spacecraft impacted Mercury's surface on 30 April 2015 following

198   a series of controlled low-altitude orbits.

199

200   **3.0 Disappearing Dayside Magnetosphere Events**

201   The strong northward magnetic field just inside the dayside magnetopause at Mercury

202   during coronal mass ejections is due to both the deep dynamo and compression-driven currents

203   on the surface of its large iron core [Hood and Schubert, 1979; Slavin et al., 2014; Jia et al, 2015;

204   Dong et al., 2019]. The net effect of these induction currents is to temporarily increase the

205   magnetic moment of Mercury from smaller amounts, ~ 5%, as it moves from lower mean solar

206   wind pressures at aphelion to higher at perihelion [Zhong et al., 2015b; Johnson et al., 2016]. Jia

207   et al. (2019) surveyed MESSENGER's four-year data set and identified 8 passes through

208   Mercury's dayside magnetosphere for which the magnetic field just inside of the magnetopause

209   exceeded 300 nT. The upstream solar wind ram pressures were estimated to range from ~ 40 to

210   90 nPa. For these pressures the magnetopause at the subsolar point would be expected to

211   approach very close to the planetary surface if it were not for the effect of the inductions

10

212 currents. Indeed, Jia et al. found that the induction currents increased the planetary magnetic

213 moment by up to ~ 25% during these most likely CME-related solar wind events [Jia et al.,

214 2019].

215   However, as illustrated in Figure 1b, magnetic reconnection at the dayside magnetopause

216 transfers magnetic flux to the nightside magnetosphere and reduces the distance from the center

217 of the nose of magnetosphere where the solar wind is "stood-off" by the planetary magnetic

218 field. In fact, Slavin and Holzer (1979) scaled Earth observations of the reduction in the radius of

219 the dayside magnetosphere due to reconnection to Mercury. This study, which predated the

220 induction analysis of Hood and Schubert (1979), predicted that the dayside magnetopause might

221 be frequently eroded to the surface when the IMF was southward and reconnection rate

222 maximized. Consistent with the predictions of both of these earlier studies, the IMF for 7 of the 8

223 highly compressed dayside magnetospheres examined by Jia et al. (2019) occurred during

224 intervals of northward IMF when erosion would be expected to be minimal.

225   Several previous studies of MESSENGER's magnetic field data have noted passes over

226 the dayside hemisphere for which no low latitude magnetopause was detected [Raines et al.,

227 2015a; Zhong et al., 2015a; Slavin et al., 2019], but no systematic or detail analysis was

228 conducted. The reason for the dayside magnetosphere being absent, or "disappearing," on such

229 occasions could be enhanced solar wind dynamic pressure that compressed the closed magnetic

230 flux down below MESSENGER's orbit or even into the low conductivity crust overlaying the its

231 highly conducting interior [see Jia et al., 2015; Dong et al., 2019]. Alternatively, reconnection-

232 driven erosion of the dayside magnetosphere could be responsible [Slavin and Holzer, 1979;

233 Slavin et al., 2009; 2010]. However, the high intensity solar wind and interplanetary magnetic

234 field (IMF) required to compress the dayside magnetic flux down into the low electrically

235   conducting crust [e.g., Hood and Schubert, 1979; Suess et al., 1979] and/or transfer the magnetic

236   flux into the magnetotail through reconnection [Slavin and Holzer, 1979] would have to be much

237   greater than the CMEs and HSS events observed early in the MESSENGER mission and

238   analyzed by Slavin et al. (2014).

239   Here we have surveyed all four years of the MESSENGER magnetometer (MAG)

240   (sample rate 20 s^{-1}) [Anderson et al., 2007] and the Fast Imaging Plasma Sensor (FIPS)

241   (complete energy per charge and composition scan of ions up to 13 keV/e in 10 s) data [Andrews

242   et al., 2007]. Due to the placement of FIPS on the MESSENGER spacecraft, full plasma

243   moments can only be derived under certain sets of assumptions [Raines et al., 2011; Gershman et

244   al., 2012; 2013; Dewey et al., 2018]. Because those assumptions are not typically met in the

245   magnetosheath plasma analyzed here, we report only energy spectra and observed densities, the

246   latter being derived from observations directly, without correction for any plasma outside the

247   field of view [Raines et al., 2013]. Heavy ions are collected into two groups by mass per charge

248   (m/q), O^+-group (m/q 16-20) and Na^+-group (m/q 21-30) [Raines et al., 2013]. All dayside passes

249   over the northern hemisphere for which the low-pass filtered B_z component of the magnetic field

250   never became positive and FIPS observed H^+ energy spectra typical of the shocked solar wind

251   making up the magnetosheath have been identified. Although there are other passes for

252   which FIPS indicates that MESSENGER did not enter the magnetosphere, here we consider only

253   the 4 pristine disappearing dayside magnetosphere events for which no magnetic fields consistent

254   with the closed dayside magnetosphere were observed in the MAG data. They occurred on 15

255   October, 2011 (or day of year (DOY) 288, 2011), 1 December (DOY 335) 2013, 13 February

256   (DOY 044) 2014, 25 March (DOY 084) 2015. Again, there are other events for which there is at

257   most only very brief encounters with closed magnetic field regions, i.e. $B_z > 0$ and FIPS

12

258   measurements of the low flux, higher energy H^+ typical of the dayside magnetosphere [Raines et

259   al., 2014; Korth et al., 2019].

260   An overview of the magnetic field measurements taken by MESSENGER on 15 October

261   2011 is displayed in Mercury Solar Magnetospheric (MSM) coordinates in Figure 3. In this

262   system the X_{MSM} axis points from the offset location of Mercury's dipole toward the Sun, the

263   Y_{MSM} axis lies in Mercury's equatorial plane and it is positive in the direction opposite to

264   planetary motion and Z_{MSM} completes the right-handed orthogonal system. The solar wind

265   aberrated frame is indicated by the primes, X'_{MSM}, Y'_{MSM} and Z'_{MSM}. Aberration is carried out

266   using Mercury's azimuthal speed about the Sun and rotating the MSM X and Y axes until X'_{MSM}

267   is opposite to an assumed mean 400 km/s radial solar wind. in the magnetic equatorial plane,

268   which is offset along Mercury's spin axis by 0.2 R_M toward the north, X_{MSM} is directed toward

269   the Sun, and Z_{MSM} complete the right-handed orthogonal system. At this stage of the mission the

270   spacecraft was still in its 12-hr orbit and two periapsis passes (at $\sim 60^o$ north latitude) occurred

271   each Earth-day. These periapses are apparent by the large amplitude maxima in the total

272   magnetic field as MESSENGER passed near the north magnetic pole in Figure 3. On this day

273   MESSENGER moved from lower to higher latitudes over the mid-morning time sector as it

274   approached its periapses. The IMF intensity at the beginning of the day was only $\sim$ 10 to 20 nT

275   and the magnetic field was relatively structureless. As indicated in Figure 3 an interplanetary

276   shock (IP SH) arrived at Mercury at $\sim$ 08:30 UTC and the IMF increased to $\sim$ 50 nT. About 3 hrs

277   later the IMF suddenly increased again to $\sim$ 90 nT and the level of fluctuations in the magnetic

278   field decreased signaling the arrival of the CME. A broader study of CME signatures in the

279   MESSENGER MAG data at Mercury, including this event, can be found in Winslow et al.

280   (2015).

13

281   The highly disturbed nature of Mercury's magnetosphere during the second pass is

282   readily apparent by comparison with the first. The periapses for these two passes occurred at

283   similar altitudes, i.e. 330 vs. 320 km, respectively. Given the mean radius of Mercury, 2440 km,

284   the change in the total magnetic field due to this small difference in periapsis altitude between

285   the two passes would be only ~ 1% as compared with the observed increase from the first to the

286   second periapsis of 15%. In addition, the magnetic field variance behind the bow shock is very

287   high for the second pass and the magnetic field intensity drops to very low levels just before

288   large amplitude magnetic field fluctuations appear. The magnetic field then becomes steady and

289   directed into the northern polar cap where a peak field of ~ 470 nT was measured. After the

290   outbound bow shock, the IMF is observed to be quite steady, but very intense with a magnitude

291   of ~ 70 nT.

292   All four of the DDM events examined here took place during coronal mass ejection that

293   were determined using the WSA-ENLIL+ Cone algorithm for these intervals on CCMC as was

294   shown earlier for the first DDM event [Odstrcil et al., 2004; Toth and Odstrcil, 1996; Baker et

295   al., 2009; 2013; Dewey et al., 2015]. Our focus is on the magnetospheric measurements made by

296   MESSENGER, but, for context, we display at the top of Figure 4 equatorial the solar wind radial

297   velocity, V_r (panel a), and the density, n (panel b) for this first event. This simulation uses CME

298   input parameters from Community Coordinated Modeling Center's (CCMC) Space Weather

299   Database Of Notifications, Knowledge, Information (DONKI; http://ccmc.gsfc.nasa.gov/donki).

300   The predicted time of arrival of the CME at Mercury is ~ 15:00 UTC or a little over 7 hrs after

301   the arrival of the IP SH. The observed arrival time of the IP SH and CME in the MESSENGER

302   data at 08:30 and 11:15 UTC are reasonably consistent with the WSA-ENLIL + Cone predictions

303   (e.g. see Dewey et al., 2015). The solar wind density dial depicts the expected compression

14

304   signatures as the higher-speed solar wind overtakes the slower solar wind. Please note that the

305   plasma density has been multiplied by the square of radial distance (in units of AU) from the

306   center of the Sun to de-trend for the decrease in density with increasing distance.

307   A zoomed-in view of the magnetic field measurements during the second periapsis pass

308   on 15 October 2011, just after the passage of the IP SH and the arrival of the CME, is shown in

309   the bottom panels of Figure 4. The three components and the total magnetic field intensity are

310   shown in panels c – f. The IMF upstream of the bow shock had an intensity of ~ 70 nT with B_z ~

311   -45 nT. Around 14:21:22 UTC the spacecraft crossed the bow shock and entered the

312   magnetosheath at an altitude of 1770 km, a magnetic latitude of 25.4^o and a local time (LT) of

313   08:10. The average intensity of the magnetic field in the magnetosheath, indicated by the

314   smoothed red trace, was ~ 200 to 220 nT, B_z ~ - 120 to -140 nT and the level of fluctuations was

315   significantly elevated over the earlier solar wind interval. The smoothed magnetic field data

316   shown with the red traces were created by performing a boxcar averaging on the magnetic field

317   data using a 40s window. Further, the fluctuations grow in amplitude as MESSENGER moved

318   toward lower altitudes and periapsis. What is most interesting about these magnetic field

319   measurements for the purpose of this study is that the mean B_z component of the magnetic field

320   did not become northward anywhere over the dayside hemisphere of Mercury during this pass.

321   The appearance of northward magnetic fields as soon as the dayside magnetopause is crossed is

322   the most fundamental and clearest signature of the dayside magnetosphere at Mercury (and

323   Earth). However, in Figure 4 the usual inbound magnetopause crossing at an altitude of ~ 1000

324   to 1500 km is not present. Rather, the magnetopause is not encountered until MESSENGER was

325   at 80° northern magnetic latitude just sunward of the terminator. Following this magnetopause

15

326 crossing the magnetic field became much steadier and stronger as the high-latitude magnetotail

327 was entered.

328   In Figure 5 the full resolution and smoothed magnetic field B_z and B-total traces for the

329 dayside passes during the 15 October 2011 and 01 December 2013 DDM events are compared

330 and contrasted. The solar wind conditions for the 2013 event were similar to those already

331 described for the 2011 event; an IP SH followed by a CME impact producing intense and very

332 disturbed planetary magnetic fields consistent with the ENLIL simulation (see Figure 4). In the

333 bottom panels of Figure 5 the similarity between these two dayside passes is quite evident. The

334 upstream IMF in both events is strong, ~ 50 to 100 nT, due to the arrival of the CME, but for the

335 2013 pass the B_z component upstream is slightly positive, but it then turns strongly southward

336 about 5 min after the bow shock is crossed to produce a magnetosheath field of B_z ~ - 200 nT. As

337 shown, the smoothed magnetic field was southward throughout the rest of the dayside pass until

338 the magnetopause is crossed at very high latitudes, i.e. at 80° north magnetic latitude. Again,

339 very large amplitude fluctuations are observed in the magnetic field until the magnetopause is

340 crossed, the magnetic field intensifies and weaken as the magnetic field becomes steadily

341 southward over the northern polar cap.

342   The other two DDM events were recorded by MESSENGER on 13 February 2014 and 25

343 March 2015 and the MAG measurements are displayed in Figure 6. Both passes were preceded

344 by IP SH's and likely CMEs, based upon the magnetic field observations and ENLIL – WSA +

345 Cone simulations (not shown). The only differences between the events in Figures 5 and 6 are:1)

346 the somewhat more intense upstream IMF intensities for the 2014 and 2015 events that

347 approached 150 nT; 2) the stronger southward B_z in the magnetosheath for these latter events, ~ -

348 300 to - 400 nT; and 3) these magnetopause crossings occurred at somewhat lower magnetic

16

349 latitudes of 66° and 76°, respectively. Note, these lower latitude magnetopause encounters,

350 presumably due to the more intense negative upstream B$_z$, also occurred at lower altitudes of ~

351 276 and 254 km, respectively, due to MESSENGER's orbit.

352

353

354

4.0 DDM Magnetosheath Plasma Observations

356   The FIPS plasma measurements for the first 3 of the DDM dayside passes are displayed

357 in Figure 7. No FIPS measurements are available for the final 25 March 2015 pass due to noise

358 generated within the instrument by penetrating solar energetic particle radiation that

359 accompanied the CME that produced this DDM event. The top panels show the FIPS H$^+$ energy

360 spectra over a 20-min interval behind the bow shock on 15 October 2011 while MESSENGER

361 was moving northward over the mid-morning dayside hemisphere (see the trajectory trace

362 labeled 288 in Figure 8). Under more typical conditions the spacecraft would have crossed the

363 magnetopause in the ~ 1200 – 1500 km altitude region. However, the H$^+$ E/q spectra in the top

364 panel and the H$^+$ density in the second panel show that MESSENGER remained in the

365 magnetosheath until the magnetopause was crossed at 14:40 UTC and the spacecraft entered the

366 high latitude magnetosphere at an altitude of 410 km and a local time of 13:00. At ~ 14:35 UTC

367 the H$^+$ density and temperature, and the He^{++} density in the third panel, increase just as the

368 amplitude and the frequency of the short duration spikes in B-total increase in panel d. It is

369 expected that the He^{++} density tracks with that of the H$^+$ since they are both of solar wind origin.

370 While He$^+$ is thought to also originate from Mercury [Raines et al., 2013], those ions have only a

17

371 very low probability of being doubly ionized so that He^{++} originating from the planet is expected

372 to be negligible. After 14:35 UTC the amplitude and frequency of occurrence of these discrete

373 magnetic structures increase as the mean magnetic field intensity increased from ~ 200 to ~ 250

374 nT and B_z decreased from ~ -100 nT to ~ -250 nT. Again, for a typical pass this is the region

375 where the spacecraft would be expected to transition from the closed dayside magnetosphere into

376 the northern cusp [e.g. Winslow et al., 2012; Raines et al., 2014; Poh et al., 2016]. Further, it is

377 in this region that Na^+-group ions are first observed during this dayside pass as displayed in the

378 panel c. This is where the cusp would usually be located and the observed 0.1-0.2 cm^{-3} densities

379 are typical of those observed in the cusp. The H^+ density and temperature begin to decrease after

380 the spacecraft passes through the magnetopause near 81 deg north magnetic latitude very near

381 where the high-latitude "back-wall" of the cusp is usually located. After MESSENGER enters

382 the high-latitude nightside magnetosphere the Na^+ density decreases and the suggestion of an

383 energy dispersion in panel (a) with the higher energy H^+ becoming depleted as the spacecraft

384 moves to lower latitudes deeper in the northern tail lobe. These observations are all consistent

385 with MESSENGER entering the plasma mantle that makes up the outer high-latitude layer of the

386 magnetotail [DiBraccio et al., 2015; Jasinski et al., 2017].

387   The FIPS measurements for the 01 December 2013 DDM pass are shown in Figure 7e-h.

388 Overall, the plasma measurements are remarkably similar to the 2011 event. Again, the

389 magnetosheath interval ends at very high latitudes with the H^+ density and temperature

390 increasing again just before passing through the magnetopause and entering the high-latitude

391 nightside magnetosphere. Na^+-group and other heavy planetary ions are observed throughout the

392 magnetosheath pass. This is observed frequently during periods of high magnetospheric activity

393 [Raines et al., 2014]. The observed densities of Na^+-group ions are typical of those passes,

18

394   though the O^+-group ion density is higher than typically observed. Finally, plasma mantle

395   density decreases and energy dispersion is observed again as MESSENGER passes more deeply

396   into the northern lobe of the magnetotail. The plasma measurements for the 13 February 2014

397   DDM magnetosheath pass are displayed in Figure 7i-l. Again, they are remarkably similar to the

398   two earlier DDM passes in almost every aspect (see the trajectory trace labelled 044 in Figure 8).

399   The trsecajectories of MESSENGER for each of the 4 DDM event passes are plotted in

400   Figure 8. The portion of each of the 4 DDM periapsis passes with MESSENGER outside of

401   Mercury's magnetosphere are plotted in red while the magnetospheric parts are in blue. The

402   orbits, plus Mercury and its magnetosphere, are then projected into the aberrated MSO Z' – X',

403   Y' – X' and Z' – Y' planes. As shown, the 4 DDM periapsis pass would certainly have detected

404   the dayside magnetosphere, if it had been present during MESSENGER's periapsis passes over

405   the northern half of the dayside hemisphere. . Further, there is general agreement as the point

406   where the high-latitude nightside magnetosphere was entered just sunward of the north magnetic

407   pole.

408

409   **5.0 DDM Flux Transfer Events**

410   When MESSENGER crossed the bow shock and entered the magnetosheath and moved

411   northward over Mercury's dayside on 15 October 2011 (see Figure 8) it not only failed to

412   encounter the usual low-to-mid-latitude magnetopause and closed dayside magnetosphere, but

413   also the steady, compressed draped IMF that makes up the PDL [Gershman et al., 2013].

414   Inspection of the high-resolution measurements of B-total for this DDM pass in Figure 9b

415   reveals that large amplitude compressive fluctuations began to increase in frequency of

19

416 occurrence and amplitude at ~ 14:30 UTC as the mean magnetic field intensity increased. These

417 fluctuations grew in amplitude as MESSENGER approached cusp latitudes similar to those seen

418 in the other 3 DDM passes in Figures 9d, f, and h. However, what stands out most are the brief,

419 several-second-long increases in magnetic field intensity that coincide with large amplitude +/-

420 B_z. These large-amplitude several second-long structures are flux transfer event (FTE) – type

421 magnetic flux ropes [Slavin et al., 2012; Imber et al., 2014].

422   The reconnection process involves the formation of multiple x-lines which fragment the

423 current sheet into flux ropes [Lee and Fu, 1985]. These very small, initially sub-ion scale flux

424 ropes then appear to grow rapidly due to both continuous reconnection at the x-lines and the

425 coalescence of adjacent flux ropes into larger flux ropes [e.g., see Akhavan-Tafti et al., 2018b].

426 FTEs have a helical topology that winds magnetic flux about an axial magnetic field near the

427 center of the structure. The axial "core" field in these FTE-type flux ropes is compressed by the

428 tension in those outer layers [Russell and Elphic, 1978; Rijnbeek et al., 1984; Zong et al., 2005;

429 Raeder, 2006; Fear et al., 2007; Hasegawa et al., 2010; Trenchi et al., 2011]. For this reason, the

430 magnetic field intensity maximizes at the center of the structure unless strong gradients in the

431 plasma pressure are present. Indeed, Gershman et al. (2016) used observations of solar energetic

432 electrons detected by FIPS while inside of Mercury's magnetosphere to confirm that FTE

433 magnetic fields are connected to the IMF. After formation, the FTEs are then carried tailward by

434 flow in the magnetosheath and pivot about the end of the magnetic fields that map to one of the

435 magnetospheric cusps as the other is transported into the magnetotail [see Cooling et al., 2001]

436   For each of the 4 DDM passes the magnetic field has been examined for the presence of

437 FTEs. They were detected based on their bipolar signature in the maximum variance component

438 of the local magnetic field (B_{max}) coinciding with a peak in both the intermediate variance

20

439   component of magnetic field (B_{int}) and $|B|$. Furthermore, we have used the Lundquist-Burlaga

440   constant-α force-free model to test that the candidate FTE's had a flux rope magnetic topology.

441   Specifically, fitting of this cylindrical force-free flux rope model to a candidate FTE with a chi-

442   square error that is less than a specified maximum is taken to indicate a successful FTE

443   identification. Further, the fitting method determines the impact parameter (i.e. closest approach

444   distance of the spacecraft trajectory to the central axis of the flux rope), the radius of individual

445   FTE-type flux rope and their axial magnetic flux [e.g., Slavin et al., 2003; DiBraccio et al., 2015;

446   Akhavan-Tafti et al., 2018]. With the assumption that the thermal pressure gradient is negligible

447   across the structure, force-free FTEs are modeled as a cylinder which contains magnetic flux that

448   is proportional to its size and core magnetic field strength. In addition, the use of the force-free

449   model enables a non-biased investigation of magnetic structures at the magnetopause. Only

450   structures that satisfy the following criteria are included in the FTE statistics for the DDM

451   events: i) Impact parameter < 0.5, ii) Chi-squared value < 0.1 (see Akhavan-Tafti et al., 2018 and

452   iii) FTE radius < 2500 km.

453   For each of the 4 DDM passes in Figure 9 there are two panels: one that graphs the

454   magnetic field intensity from before the bow shock to a little after the magnetopause crossing to

455   the nightside high-latitude magnetosphere and a second that plots the number of FTEs identified

456   per 30 sec accumulation intervals. The trajectories for the DDM passes in Figure 8 show that

457   MESSENGER's orbit is providing latitude scans of the frequency of occurrence for the FTEs.

458   Indeed, for these DDM intervals MESSENGER remained in the magnetosheath from near-

459   equatorial latitudes up to ~ 80°. The frequency of occurrence panels in Figure 9 show that the

460   number of FTEs increase from a few per 30 sec bin in the high-altitude magnetosheath just inside

461   the bow shock at low latitudes to a highly reproducible peak of ~ 15 per 30 sec, or 30 FTEs/min,

21

462   at cusp latitudes. A maximum near the cusp is expected because one end of each of these FTE-

463   type flux ropes must map to the north magnetic pole and pivot about the cusp as they are carried

464   tailward by the flow of shocked solar wind in the magnetosheath. And, the highest rate of FTE

465   occurrence is indeed at cusp latitudes during these DDM passes.

466   The physical properties of the 438 FTE-type flux ropes identified in the DDM passes are

467   displayed as histograms in Figure 10 and have been fit with exponentials. The mean radius for

468   these FTEs is 203 km, which is ~ 10 times the estimated solar wind ~ 1 keV H^+ gyro-radius just

469   inside high-pressure magnetopause crossings [Slavin et al., 2014; Jia et al., 2019] and their mean

470   magnetic flux content is 32 kWb. With these FTEs being swept into the magnetotail at a rate of

471   0.5 sec^{-1} their mean contribution to Mercury's cross-magnetospheric potential drop is 16 kV.

472   This value is about half of the total potential drops estimated from the Dungey cycle loading-

473   unloading of the tail with magnetic flux [Slavin et al, 2010; Imber and Slavin, 2017] and the

474   energy dispersion in the plasma mantle ions [DiBraccio et al., 2015; Jasinski et al., 2018].

475   Further, this FTE flux transfer rate is comparable to that estimated for the non-FTE B_n magnetic

476   flux being transferred to the magnetotail [Slavin et al., 2009; DiBraccio et al., 2013; Imber et al.,

477   2014]. Alternatively, if we take half of the typical Dungey cycle, ~ 90 sec [Imber and Slavin,

478   2017], to be the time it takes to cycle all of the FTEs at the dayside magnetopause into the tail,

479   then the total magnetic flux contained in all dayside FTEs at a given moment is ~ 90 sec x 16

480   kWb/sec or ~ 1.4 MWb. This compares with typical tail lobe magnetic flux contents of ~ 2.5 to 3

481   MWb [Slavin et al., 2012; Johnson et al., 2012] and a total planetary magnetic flux closing

482   exterior to Mercury of $2\pi M_o/R_M$ or 7 – 9 MWb depending upon the Mercury magnetic moment

483   value assumed [Slavin et al., 2009; 2010].

484

22

6.0 DDM Magnetopause Analysis

485

486   The MESSENGER magnetic field data for the DDM magnetopause crossings are

487   displayed in more detail in Figures 11 and 12. In each instance the crossing interval is marked by

488   two blue vertical dashed lines. Given the presence of large amplitude FTEs and cusp plasma

489   filaments [Poh et al., 2016], the red trace graphs the magnetic field smoothing using 40 sec

490   boxcar averages. The magnetic field measurements from 14:37 to 14:43 UTC during the first

491   DDM pass on 15 October 2011 are displayed in Figure 11 a - d. The magnetosheath data on the

492   left hand-side has frequent, large amplitude fluctuations, many of which are flux transfer events

493   that were analyzed and discussed in the previous section. As expected for a CME-impact interval

494   the magnetic field intensities outside and inside of the magnetopause are of similar intensities at

495   ~ 300 and 400 nT [see Slavin et al., 2014], respectively, presumably due to low upstream

496   Alfvénic Mach numbers [Gershman et al., 2013]. A number of magnetopause current sheet

497   crossings are present between ~ 14:39 and 14:41 UTC and set off with vertical dashed lines.

498   Minimum variance analysis (MVA) was performed on the 1 sec resolution smoothed

499   MAG data shown in Figure 11. The minimum, intermediate and maximum variance

500   Eigenvectors are well defined with intermediate to minimum and maximum and intermediate

501   Eigenvalue ratios of 16 and 80, respectively. The Eigenvectors in solar wind aberrated MSM

502   coordinates are shown in Figure 11 and the ratio of the magnetic field component normal to the

503   magnetopause to the magnetic field just inside the current layer, $\alpha = B_N/B_{MP}$, which is a measure

504   of the reconnection rate, is 0.12, are displayed in Table 1. This value is comparable to the ratios

505   determined for the dayside magnetopause at Mercury in previous studies [Slavin et al., 2008;

506   2009; DiBraccio et al., 2013; Liljeblad et al., 2016; Jia et al., 2019; Dong et al., 2019].

23

507   The normal component of the magnetic field to the magnetopause, B_N, the dimensionless

508   reconnection rate, α, the dynamic pressure, P_{sw}, and the subsolar standoff distance of the

509   magnetopause, R_{ss}, are summarized in Table 1. They were determined using the same methods

510   and expressions as used in earlier studies of the highly compressed magnetosphere (HCM)

511   events in the MESSENGER data [Slavin et al., 2014; Jia et al., 2019]. Upstream solar wind

512   speeds are generally not measured by MESSENGER, but the locations of the magnetopause

513   crossings in MSM have been aberrated assuming typical solar wind speeds of 400 km/sec and

514   Mercury azimuthal orbital speeds as a function of distance from the Sun. Average magnetopause

515   position for each of these events is given in Table 1 using this aberrated system (X'_{MSM}, Y'_{MSM} ,

516   Z'_{MSM}) in the fifth column from the left.

517   Figure 11e-h shows the magnetic field measurements of the magnetopause crossing from

518   01:35 to 01:39 UTC on 01 December 2013. Unlike the magnetopause crossing on 15 October

519   2011, the magnetic field magnitude difference between the magnetosheath and dayside

520   magnetosphere magnetic field is greater, by ~ 200 nT, which suggests a higher Alfvenic Mach

521   number than the 2011 event. MVA is also performed on the smoothed magnetic field

522   measurements (red line) of the magnetopause crossing interval delimited by dashed blue lines.

523   The eigenvectors are well-defined with intermediate to minimum and maximum and

524   intermediate eigenvalue ratios of ~ 5 and 303, respectively, and a slightly higher reconnection

525   rate of ~ 0.16.

526   The magnetic field observations for the 13 February 2014 and 25 March 2015

527   magnetopause crossings are displayed in Figure 12. Overall, these events are quite similar

528   despite differences in the CMEs and the altitudes at which the transitions from the

529   magnetosheath to the magnetosphere occurred (e.g. the 25 March 2015 measurements were taken

24

530   at an altitude of just ~ 50 km). The magnetic field intensities in the magnetosheath for these two

531   events were ~ 50 to 70% of the total magnetic field just inside of the magnetosphere. Frequent

532   large amplitude fluctuations are evident in the magnetosheath, but short duration, deep decreases

533   in the magnetic field intensity, which Slavin et al. (2014) and Poh et al. (2016) termed cusp

534   filaments are present immediately after MESSENGER entered the magnetosphere. As with the

535   2011 and 2013 magnetopause crossings, the Eigenvectors are well defined for both the 2014 and

536   2015 events. In these cases, the intermediate to minimum and maximum and intermediate

537   Eigenvalue ratios were ~ 10 and 23 and ~ 9 and 69, respectively. Similarly, the ratios of the

538   magnetic field component normal to the magnetopause to the magnetic field just inside the

539   current layer are 0.17 and 0.29 for the 2014 and 2015 events, respectively.

540   The upstream solar wind pressure, P_{sw}, must be derived from the state of compression of

541   planetary magnetic field [Slavin et al., 2014] because of the FIPS field-of-view limitations

542   imposed by MESSENGER's thermal sun shade. The WSA-ENLIL + Cone simulation [Odstrcil

543   et al., 2004; Toth and Odstrcil, 1996; Zhao et al., 2002] was used to provide valuable context

544   regarding the presence of high-speed streams and coronal mass ejections, but the uncertainties in

545   the predictions themselves and the typical timing errors surrounding arrival times [e.g. Dewey,

546   2015] are too large to support the sorts of quantitative studies conducted here. For this reason,

547   we, again, follow the methodology of Slavin et al. (2014) and Jia et al. (2019) and assume a

548   Newtonian pressure balance across the magnetopause, the MVA magnetopause normals, and the

549   assumption, based upon the FIPS data, that the plasma pressure in the outer dayside

550   magnetosphere is very small compared to the magnetic pressure [Raines et al., 2015]. In this

551   case the solar wind pressure computed from the pressure balance condition becomes [Spreiter et

552   al., 1966]:

25

553 $$P_{sw} = (B^2/2\mu_o)/(0.88\cos^2\vartheta) \qquad (1)$$

554 where ϑ in the angle between the magnetopause unit normal and the upstream solar wind

555 velocity vector, which is assumed to be radially outward from the Sun, and 0.88 is effectively a

556 drag coefficient determined from numerical gas dynamic numerical modeling for blunt obstacles

557 [Spreiter et al., 1966]. Methods similar to these have been used previously for Earth [e.g. Holzer

558 and Slavin, 1978] and other planets [Slavin et al., 1979; 1985; Crider et al., 2003]. The upstream

559 solar wind pressures inferred for the DDM passes in this manner as listed in Table 1 were 142,

560 182, 289 and 233 nPa for the 2011, 2013, 2014 and 2015 events. Similarly, the dimensionless

561 reconnection rates, B_N/B_{MP}, for these events were 0.12, 0.16, 0.17 and 0.29, respectively. The

562 mean is 0.19, which is somewhat greater than the mean of rate of 0.13 determined from a larger

563 ensemble of magnetopause crossings by DiBraccio et al. (2013).

564

565 **7.0 Discussion**

566 The mean bow shock and magnetopause nose distances determined from the complete set

567 of MESSENGER boundary crossings are ~ 1.9 R_M and 1.45 R_M, respectively [Winslow et al.,

568 2013]. In Figure 13 the DDM event bow shock and magnetopause crossings have been plotted in

569 solar wind aberrated cylindrical MSM coordinates. The best fits obtained by Winslow et al.

570 (2013) to the complete MESSENGER bow shock data set and our fits to the 8 DDM shock

571 crossings are shown in gray and red, respectively. For both data sets the Mercury bow shock

572 crossings have been fit using the offset conic surface method of Slavin et al. (1981). The shock

573 surfaces for the total MESSENGER data set and the DDM events do not differ greatly in shape,

574 but the nose, or stand-off distance, for the DDM bow shock is much closer at 1196 km, or ~ 0.5

26

575   R_M. Global magnetohydrodynamic or hybrid modeling of the DDM intervals is planned as part

576   of a future study, but the large planetward shift of the bow shock location during these DDM

577   intervals strongly suggests that the solar wind streamlines in the subsolar region intersect the

578   surface. If this is correct, then solar wind impact will take place over some or much of the

579   dayside surface during these DDM events, especially given the low Alfvénic Mach numbers

580   expected during CME impacts [see Slavin et al., 1980; 1981].

581   The 8 DDM magnetopause crossings have been fit to the Shue model surface [Shue et al.,

582   1997]:

583                           $r = R_{SS} \left[2/(1 + \cos\theta)\right]^b$ (2)

584   where θ is the solar zenith angle from the subsolar point, the magnetopause shape parameter, b,

585   and the solar wind stand-off distance R_{ss} from the center of the obstacle. The mean DDM bow

586   shock surface model for all of the MESSENGER magnetopause crossings was determined to b =

587   0.5 and $R_{ss} = 1.4\ R_M$ [Winslow et al., 2013]. Our best fit of the DDM magnetopause crossings to

588   the Shue surface is shown in solid blue in Figure 13. This surface is quite different from the

589   mean determined for all conditions (see gray solid line in Figure 13) with b = 0.7 and $R_{SS} = 0.65$

590   R_M. Not only is the DDM magnetopause more flared, but it passes below the surface of Mercury

591   forward of the terminator plane in the northern hemisphere and just tailward in the southern

592   hemisphere. Note also in Figure 13 that the magnetopause normal determined using MVA

593   analysis (see Figures 11 and 12) are also displayed as arrows in Figure 13 at the point where the

594   crossings occurred. As shown these MVA magnetopause normal vectors are very close to

595   expectations based upon the DDM magnetopause model.

27

596   Our analyses of the 4 disappearing dayside magnetosphere events that we identified in

597   the MESSENGER four-year data set are summarized in Figure 14. The solar wind dynamic

598   pressure is shown on the vertical axis and the distance to the nose of the magnetopause, R_{ss}, is on

599   the horizontal axis. In addition to the DDM events, the 8 highly compressed magnetosphere

600   events from Jia et al. (2019) are displayed for comparison. Here the P_{SW} and R_{SS} values for all 12

601   events are plotted in same manner as in Jia et al. (2019).

602   We note, first, that the HCM event solar wind pressures and R_{SS} values range from ~ 44

603   nPa to ~ 93 nPa and 1.25 to 1.03 R_M, respectively [Jia et al., 2019]. In contrast, the solar wind

604   pressures for the DDM events are much larger at ~ 142 to ~ 289 nPa (see Table 1). The

605   Chapman-Ferraro (C-F) sixth-root of P_{sw} relationship [Chapman and Ferraro, 1932] with solar

606   wind stand-off distance for a ~ 200 nT- R_M^3 magnetic moment is displayed as a thin dashed gray

607   line. Note that this relationship should hold not only in the absence of reconnection at the

608   magnetopause or induction inside of Mercury, but also if these effects counter-balance each other

609   [Slavin et al., 2014]. The P_{sw} – R_{ss} relationship derived by Glassmeier et al. (2007), which

610   includes the effects of induction but not reconnection in Mercury's interior, is shown as a bold

611   dashed line to the right to the right of the C-F curve. The Chapman-Ferraro model predicts that

612   the nose of the magnetopause should be compressed down to Mercury's surface for a solar wind

613   dynamic pressures of ~ 90 nPa. This pressure increases to ~ 200 to 250 nPa when the effects of

614   induction currents on the surface of Mercury's iron core at taken into account [Hood and

615   Schubert, 1979; Glassmeier et al., 2007]. By comparison, the typical solar wind stand-off

616   distance for the nose of Mercury's magnetopause is only ~ 1.4 to 1.5 R_M from the center of the

617   planet for an average solar wind pressure of ~ 10 – 15 nPa [Winslow et al., 2013].

28

618   The size of the boxes in Figure 14 represent the individual magnetopause crossings and

619   they are proportional to the dimensionless reconnection rate, $\alpha = B_N/B_{MP}$, determined for each

620   magnetopause crossing from the MVA analysis as described in DiBraccio et al. (2013). As

621   shown, the dimensionless reconnection rates ranged from 0.01 to 0.29 with the lower rates

622   corresponding mostly to the HCM events and the highest rates to the DDM events. This result is

623   likely due to reconnection at the DDM magnetopause crossings being more symmetric, i.e. the

624   ratio of the magnetosheath to the magnetospheric magnetic field intensity being closer to unity

625   during the larger, more impactful CME producing DDMs.

626   The magnetopause crossings in Figure 14 with the highest reconnection rates, i.e. the

627   mostly larger boxes, are associated with the DDM events and these events are located to the left

628   of the C-F curve and they have extrapolated subsolar points below the surface, i.e. $R_{SS} < 1$ (see

629   Figure 13). In contrast the HCM events with the highest magnetopause reconnection rates are

630   located closer to the Chapman-Ferraro curve and the crossings with the smallest dimensionless

631   reconnection rates are located closest to the Glassmeier et al. curve on the right-hand side that

632   includes the effects of induction. Overall these results suggest that reconnection-driven dayside

633   magnetic flux transfer to the magnetotail and the addition of closed magnetic flux to the dayside

634   magnetosphere due to induction currents are in approximate balance for these highly compressed

635   dayside magnetosphere events. For this reason, the HCM events do not appear to expose the

636   dayside to direct solar wind impact, i.e. their R_{ss} values are greater than 1, for the HCM events.

637   These conclusions are strongly supported by the global MHD simulations of the solar wind

638   interaction with Mercury's magnetic field and conducting iron core by Jia et al. (2019).

639   In contrast to the HCM events, the DDM events have R_{ss} values a between 0.61 and 0.66

640   (see Table 1) indicating that most of dayside hemisphere experiences direct solar wind impact. If

29

641   these events were primarily ue to compression of the closed magnetic flux down into the crust,

642   then a clustering near $R_{ss} \sim 1$ would have been expected in Figure 14 because the solar wind

643   cannot exert pressure below the surface due to its absorption and neutralization upon contact

644   with the regolith. For this situation the bow shock would be expected to be located closer to the

645   planet than would be the case if all of the solar wind were deflected by a magnetopause. The

646   reason is simply that some or many of the solar wind flow stream lines would intersect and

647   terminate in Mercury's surface as opposed to requiring that a more distant bow shock and thicker

648   magnetosheath would allow all of them to be deflected about the magnetopause (e.g. see Spreiter

649   et al., 1966; Slavin et al., 1980).

650   Though heavy ions were present in each of the three events for which plasma data was

651   available, substantially more Na^+-group ions were observed throughout the magnetosheath

652   passage on DOY 335 2013. Raines et al. (2014) hypothesized that the >500 eV heavy ions

653   typically observed in Mercury's northern cusp are energized from < 1 eV photo-ions as part of

654   the reconnection process on the dayside magnetopause. As this event is also the one with the

655   highest FTE rate observed throughout the magnetosheath, it is consistent with that hypothesis.

656   The enhanced heavy ion content on DOY 335 2013 is not likely due to seasonal effects (local

657   time). Those effects showed maximum heavy ions in orbits that passed through the dayside

658   close to local times 0900 and 1500, whereas this event passes through at nearly 1200.

659   The relative contributions of solar wind compression and reconnection-driven erosion to

660   the disappearance of the dayside magnetosphere at the $\sim$ 250 to 400 km altitudes of the

661   MESSENGER passes studied here is difficult to determine. The very high solar wind pressures

662   inferred from our analyses of the DDM high-latitude magnetopauses are near those required to

663   compress the closed dayside magnetic fields until it is trapped between the incident solar wind

30

664 and the highly electrically conducting iron core (see Figures 1). However, the southward IMF in

665 the dayside magnetosheath are equally impressive with $B_z \sim -100$ to -400 nT and very high rates

666 of FTE-type flux ropes are observed in the magnetosheath as discussed earlier. If the closed

667 field lines on the dayside are eroded by reconnection, i.e. opened and transferred to the lobes of

668 the tail, then the high-latitude magnetopause crossings might be expected to move equatorward,

669 enhanced flaring of the tail magnetopause would take place and the lobe magnetic flux content

670 would be enhanced. As described earlier, there is evidence for each of these effects, but the

671 results are not so clear as those for the extreme solar wind pressure enhancements. Planned

672 studies beyond the scope of the analyses presented here will expand beyond the very pristine

673 disappearing dayside magnetosphere events considered here to include events with a wider range

674 of IMF orientations and intervals when closed magnetospheric intervals on the dayside are

675 briefly observed in between intervals of low-altitude magnetosheath.

676

677 **9.0 Conclusions**

678 The primary features of the disappearing dayside magnetosphere events are illustrated in

679 Figure 15. The magnetic field lines due to the core dynamo and the induction currents on the

680 core surface, are shown in yellow and green, respectively. During the disappearing dayside

681 magnetosphere examined here MESSENGER remained in the magnetosheath even at altitudes as

682 low as $\sim 250 - 300$ km at latitudes below $\sim 80^{\circ}$. We cannot rule out the existence of some closed

683 dayside magnetic flux above the surface during these DDM intervals. However, the extremely

684 high solar wind dynamic pressures, more than 2 orders of magnitude above typical levels, the $\sim -$

685 100 to -400 nT southward magnetic fields in the magnetosheath and the large amount of

31

686   magnetic flux contained in FTE-type flux ropes at any given moment, comparable to half of the

687   total open flux in the tail lobes, all argue against a reservoir of closed magnetic flux below the ~

688   400 to 250 km altitudes of MESSENGER during these DDM dayside passes. Further, as

689   illustrated in Figure 15, the extreme closeness of the bow shock especially in the subsolar region

690   suggests continued direct solar wind impact and absorption on the surface, as opposed to

691   complete diversion about Mercury. Indeed, it is interesting to speculate that terrestrial-type

692   exoplanets orbiting close to low-mass stars, e.g. "hot-Earths", may often have the ability of their

693   planetary magnetic fields to shield atmospheric neutrals seriously compromised by the same

694   combination of extreme stellar wind ram pressure and interplanetary magnetic intensity as found

695   here at Earth during DDM events [e.g. Dong et al, 2017].

696   There are many important questions regarding these DDM intervals that remain to be

697   understood. The relative amounts of magnetic flux created by induction currents flowing on the

698   surface of the planet's iron core, compressed into the crust by the high solar wind pressure,

699   sequestered in the large numbers of FTE-type flux ropes and/or transferred to the magnetotail by

700   reconnection-driven erosion of the dayside magnetosphere. Further, the reasons for the very high

701   reconnection rates determined for the DDM high-latitude magnetopause crossings, i.e. by a

702   factor of nearly 50% higher than the mean for the highly compressed magnetosphere intervals

703   analyzed by Jia et al. (2019) are not known. Indeed, the region(s) where the large numbers of

704   FTE-type flux ropes formed during these DDMs, e.g. very low altitude/low latitude closed

705   magnetic fields or at higher latitudes closer to the polar or flank terminator plane, is not

706   understood at all. If direct solar wind impact is as extensive as suggested by Figure 15, then the

707   contribution of solar wind-driven sputtering to Mercury's exosphere should maximize during

708   DDM events. Indeed future studies of these DDM events, and others that are more complex (e.g.

32

709 time dependent or shorter duration) and more frequent than the pristine examples examined here,

710 using global numerical magnetospheric simulations will be necessary before the impact of DDM

711 events on the short- and longer-term solar wind flux reaching Mercury's surface and their role in

712 supporting the neutral exosphere and magnetospheric heavy ion populations through sputtering

713 can be assessed [Killen et al., 2019; Korth et al., 2019]. The joint ESA – JAXA – NASA

714 BepiColombo mission is scheduled to arrive at Mercury in late 2025. The dual-spacecraft

715 observations to be returned by this mission will likely provide much new data on the sources of

716 Mercury's exospheric neutrals and magnetospheric ions.

717

727

728 11.0 References

729 Akhavan-Tafti, M., Slavin, J. A., Le, G., Eastwood, J. P., Strangeway, R. J., Russell, C. T.,

33

730   et al. (2018). MMS examination of FTEs at the Earth's subsolar magnetopause. Journal

731   of Geophysical Research: Space Physics, 123. https://doi.org/10.1002/2017JA024681

732   Alexeev, I. I., Belenkaya, E. S., Slavin, J. A., Korth, H., Anderson, B. J., Baker, D. N., Boardsen,

733   S. A., Johnson, C. L., Purucker, M. E., Sarantos, M. and Solomon, S. C. (2010). Mercury's

734   magnetospheric magnetic field after the first two MESSENGER flybys. Icarus, 209, 23–39,

735   doi:10.1016/j.icarus.2010.01.024. 2010

736   Anderson, B. J., Acuña, M. H., Lohr, D. A., Scheifele, J., Raval, A., Korth, H. and Slavin, J. A.

737   (2007). The Magnetometer instrument on MESSENGER. Space Sci. Rev., 131, 417–540,

738   doi:10.1007/s11214-007–9246-7.

739   Anderson, B. J., Johnson, C. L., Korth, H., Purucker, M. E., Winslow, R. M., Slavin, J. A.,

740   Solomon, S. C., McNutt, R. L., Jr., Raines, J. M. and Zurbuchen, T. H. (2011). The global

741   magnetic field of Mercury from MESSENGER orbital observations, *Science*, **333**, 1859–

742   1862. doi:10.1126/science.1211001.

743   Andrews, G. B., Zurbuchen, T. H., Mauk, B. H., Malcom, H., Fisk, L. A., Gloeckler, G., Ho, G.

744   C., Kelley, J. S., Koehn, P. L., LeFevere, T. W., Livi, S. S., Lundgren, R. A. and Raines, J.

745   M. (2007). The Energetic Particle and Plasma Spectrometer instru- ment on the

746   MESSENGER spacecraft. Space Sci. Rev., 131, 523–556, doi:10.1007/s11214-007–9272-5.

747   Baker, D. N., Odstrcil, D., Anderson, B. J., Arge, C. N., Benna, M., Gloeckler, G., Raines, J. M.,

748   Schriver, D., Slavin, J. A., Solomon, S. C., Killen, R. M. and Zurbuchen, T. H. (2009). Space

749   environment of Mercury at the time of the first MESSENGER flyby: Solar wind and

750   interplanetary magnetic field modeling of upstream conditions. J. Geophys. Res., 114,

751   A10101, doi:10.1029/2009JA014287.

34

752   Baker, D. N., Poh, G. K., Odstrcil, D., Arge, C. N., Benna, M., Johnson, C. L., Korth, H.,

753   Gershman, D. J., Ho, G. C., McClintock, W. E., Cassidy, T. A., Merkel, A., Raines, J. M.,

754   Schriver, D., Slavin, J. A., Solomon, S. C., Trávníček, P. M., Winslow, R. M. and

755   Zurbuchen, T. H. (2013). Solar wind forcing at Mercury: WSA-ENLIL model results. J.

756   Geophys. Res. Space Physics, 118, 45–57, doi:10.1029/2012JA018064.

757   Benna, M., Anderson, B. J., Baker, D. N., Boardsen, S. A., Gloeckler, G., Gold, R. E., Ho, G. C.,

758   Killen, R. M., Korth, H., Krimigis, S. M., Purucker, M. E., McNutt, R. L., Jr., Raines, J. M.,

759   McClintock, W. E., Sarantos, M., Slavin, J. A., Solomon, S. C. and Zurbuchen, T. H. (2010).

760   Modeling of the magnetosphere of Mercury at the time of the first MESSENGER flyby.

761   Icarus,

762   209, 3–10, doi:10.1016/j.icarus.2009.11.036.

763   Borovsky, J. E., Nemzek, R. J. and Belian, R. D. (1993). The occurrence rate of magnetospheric-

764   substorm onsets: Random and periodic substorms. J. Geophys. Res., 98,3807–3813,

765   doi:10.1029/92JA02556.

766   Chané, E., J. Saur, F. M. Neubauer, J. Raeder, and S. Poedts (2012), Observational evidence of

767   Alfvén wings at the Earth, J. Geophys. Res.,117, A09217, doi:10.1029/2012JA017628.

768   Chapman, S. and V. C. A. Ferraro (1932), A new theory of magnetic storms, pt. 1, The initial

769   phase, Terr. Mag., 37, 147-156.

770   Cooling, B. M. A., Owen, C. J. and Schwartz, S. J. (2001). Role of the magnetosheath flow in

771   determining the motion of open flux tubes. J. Geophys. Res., 106, 18,763–18,776,

772   doi:10.1029/2000JA000455.

35

773 Crider, D. H., D. Vignes, A. M. Krymskii, T. K. Breus, N. F. Ness, D. L. Mitchell, J. A. Slavin,

774 and M. Acuña (2003) A proxy for determining solar wind dynamic pressure at Mars using

775 Mars Global Surveyor data, J. Geophys. Res., 108 (A12), 1461, doi:10.1029/2003JA009875.

776

777 DiBraccio, G. A., Slavin, J. A., Boardsen, S. A., Anderson, B. J., Korth, H., Zurbuchen, T. H.,

778 Raines, J. M., Baker, D. N., McNutt, R. L., Jr. and Solomon, S. C. (2013). MESSENGER

779 observations of magnetopause structure and dynamics at Mercury. J. Geophys. Res. Space

780 Physics, 118, 997–1008, doi:10.1002/ jgra.50123.

781 DiBraccio, G. A., Slavin, J. A., Raines, J. M., Gershman, D. J., Tracy, P. J., Boardsen, J. A.,

782 Zurbuchen, T. H., Anderson, B. J., Korth, H., McNutt, R. L., Jr. and Solomon, S. C. (2015b).

783 First observations of Mercury's plasma mantle by MESSENGER. Geophys. Res. Lett., 42,

784 9666–9675, doi:10.1002/2015GL065805.

785 Domingue, D. L., Chapman, C. R., Killen, R. M., Zurbuchen, T. H., Gilbert, J. A., Sarantos, M.,

786 Benna, M., Slavin, J. A., Schriver, D., Trávníček, P. M., Orlando, T. M., Sprague, A. L.,

787 Blewett, D. T., Gillis-Davis J. J., Feldman, W. C., Lawrence, D. J., Ho, G. C., Ebel, D. S.,

788 Nittler, L. R., Vilas, F., Pieters, C. M., Solomon, S. C., Johnson, C. L., Winslow, R. M.,

789 Helbert, J., Peplowski, P. N., Weider, S. Z., Mouawad, N., Izenberg, N. R. and McClintock,

790 W. E. (2014). Mercury's weather-beaten surface: Understanding Mercury in the context of

791 lunar and asteroidal space weathering studies. Space Sci. Rev., 181, 121–214,

792 doi:1J0.1007/s11214-014–0039-5.

793 Dong, C. F., M. Lingam, Y. J. Ma, and O. Cohen, Is Proxima Centauri B habitable? A study of

794 atmospheric loss, ApJ Letters, 837, L26 (2017).

36

795   Dong, C. F., L. Wang, A. Hakim, A. Bhattacharjee, J. A. Slavin, G. A. DiBraccio, K.

796   Germaschewski, A Novel Ten-Moment Multifluid Model for Mercury: From the Planetary

797   Conducting Core to the Dynamic Magnetosphere, arXiv:1904.02695 (2019).

798   Dungey, J. W. (1961). Interplanetary magnetic field and the auroral zones. Phys. Rev. Lett., 6,

799   47.

800   Exner, X., D. Heyner, L. Liuzzo, U. Motschmann, D. Shiota, K. Kusano, and T. Shibayama

801   (2018), Coronal mass ejection hits mercury: A.I.K.E.F. hybrid-code results compared to

802   MESSENGER data, https://doi.org/10.1016/j.pss.2017.12.016

803   Fear, R. C., Milan, S. E., Fazakerley, A. N., Owen, C. J., Asikainen, T., Taylor, M. G. G. T.,

804   Lucek, E. A., Rème, H., Dandouras, I. and Daly, P. W. (2007). Motion of flux transfer

805   events: A test of the Cooling model. Ann. Geophys., 25, 1669–1690, doi:10.5194/angeo-25–

806   1669-2007.

807   Gershman, D. J., Slavin, J. A., Raines, J. M., Zurbuchen, T. H. Anderson, B. J., Korth, H., Baker,

808   D. N. and Solomon, S. C. (2013). Magnetic flux pileup and plasma depletion in Mercury's

809   subsolar   magnetosheath.   J.   Geophys.   Res.   Space   Physics,   118,   7181–7199,

810   doi:10.1002/2013JA019244.

811   Gershman, D. J., Dorelli, J. C., DiBraccio, G. A., Raines, J. M., Slavin, J. A., Poh, G. and

812   Zurbuchen, T. H. (2016). Ion-scale structure in Mercury's magnetopause reconnection

813   diffusion region. Geophys. Res. Lett., 43, 5935–5942, doi:10.1002/ 2016GL069163.

814   Glassmeier, K.-H., Grosser, J., Auster, U., Constantinescu, D., Narita, Y. and Stellmach, S.

815   (2007). Electromagnetic induction effects and dynamo action in the Hermean system. Space

816   Sci. Rev., 132, 511–527, doi:10.1007/s11214-007–9244-9.

817   Hasegawa, H., Wang, J., Dunlop, M. W., Pu, Z. Y., Zhang, Q.-H., Lavraud, B., Taylor, M. G. G.

818   T., Constantinescu, O. D., Berchem, J., Angelopoulos, V., McFadden, J. P., Frey, H. U.,

819   Panov, E. V., Volwerk, M. and Bogdanova, Y. V. (2010). Evidence for a flux transfer event

820   generated by multiple X-line reconnection at the magnetopause. Geophys. Res. Lett., 37,

821   L16101, doi:10.1029/2010GL044219.

822   Heyner, D., Nabert, C., Liebert, E. and Glassmeier, K.-H. (2016). Concerning reconnection-

823   induction balance at the magnetopause of Mercury. J. Geophys. Res. Space Physics, 121,

824   2935–2961, doi:10.1002/2015JA021484.

825   Holzer, R. E., and J. A. Slavin (1978), Magnetic flux transfer associated with expansions and

826   contractions of the dayside magnetosphere, J. Geophys. Res., 83, 3,831.

827   Hood, L. and Schubert, G. (1979). Inhibition of solar wind impingement on Mercury by

828   planetary induction currents. J. Geophys. Res., 84, 2641–2647,

829   doi:10.1029/JA084iA06p02641.

830   Imber, S. M., Slavin, J. A., Boardsen, S. A., Anderson, B. J., Korth, H., McNutt, R. L., Jr. and

831   Solomon, S. C. (2014). MESSENGER observations of large dayside flux transfer events: Do

832   they drive Mercury's substorm cycle? J. Geophys. Res. Space Physics, 119, 5613–5623,

833   doi:10.1002/2014JA019884.

834   Imber, S. M., J. A. Slavin, S. A. Boardsen, B. J. Anderson, H. Korth, R. L. McNutt, Jr., and S. C.

835   Solomon (2014), MESSENGER observations of large dayside flux transfer events: Do they drive

836   Mercury's substorm cycle?, J. Geophys. Res. Space Physics, 119, 5613–5623,

837   doi:10.1002/2014JA019884.

838 Janhunen, P. and Kallio, E. (2004). Surface conductivity of Mercury provides current closure and

839   may affect magnetospheric symmetry. Ann. Geophys., 22, 1829–1830, doi:10.5194/angeo-22–

840   1829-2004.

841 Jasinski, J. M., Slavin J. A., Raines J. M. and DiBraccio G. A. (2017). Mercury's solar wind

842   interaction as characterized by magnetospheric plasma mantle observations with MESSENGER.

843   Journal of Geophysical Research: Space Physics, 122. https://doi.org/10.1002/2017JA024594

844 Jia, X., Slavin, J. A., Gombosi, T. I., Daldorff, L. K. S., Toth, G., & van der Holst, B. (2015).

845   Global MHD simulations of Mercury's magnetosphere with coupled planetary interior: Induction

846   effect of the planetary conducting core on the global interaction. J. Geophys. Res., 120 , 4763-

847   4775. doi:10.1002/2015JA021143

848 Jia, X., Slavin, J. A., Poh, G., DiBraccio, G. A., Toth, G., Chen, Y., et al. (2019). MESSENGER

849   observations and global simulations of highly compressed magnetosphere events at Mercury.

850   Journal of Geophysical Research:Space Physics, 124. https://doi.org/10.1029/2018JA026166.

851 Johnson, C. L., M. E. Purucker, H. Korth, B. J. Anderson, R. M. Winslow, M. M. H. Al Asad,

852   J. A. Slavin, I. I. Alexeev, R. J. Phillips, M. T. Zuber, and S. C. Solomon (2012),

853   MESSENGER observations of Mercury's magnetic field structure, J. Geophys. Res. – Space

854   Physics, 117, E00L14, doi:10.1029/2012JE004217.

855 Johnson, C. L., L. C. Philpott, B. J. Anderson, H. Korth, S. A. Hauck, II, D. Heyner, R. J.

856   Phillips, R. M. Winslow, and S. C. Solomon (2016), MESSENGER observations of induced

857   magnetic fields in Mercury's core, Geophys. Res. Lett., 43, 2436–2444,

858   doi:10.1002/2015GL067370.

859   Kabin, K., Gombosi, T. I., DeZeeuw, D. L. and Powell, K. G. (2000). Interaction of Mercury

860   with the solar wind. Icarus, 84, 397–406, doi:10.1006/icar.1999.6252.

861   Kidder, A., Winglee, R. M. and Harnett, E. M. (2008). Erosion of the dayside magnetosphere at

862   Mercury in association with ion outflows and flux rope generation. J. Geophys. Res., 113,

863   A09223, doi:10.1029/2008JA013038.et al., 2008

864   Killen, R. M., M. H. Burger, R. J. Vervack, Jr, and T. A. Cassidy (2019), Understanding

865   Mercury's Exosphere: Models derived from MESSENGER observations, *Mercury: The View*

866   *After MESSENGER*, eds. S. C., L. R. Nittler, and B. J. Anderson, London: ISBN: 978-

867   1107154452.

868   Koth, H., B. J. Anderson, C. L. Johnson, J. A. Slavin, J. M. Raines, and T. H. Zurbuchen (2019),

869   Structure and Configuration of Mercury's Magnetosphere, in Mercury: The view after

870   MESSENGER, eds. S. C., L. R. Nittler, and B. J. Anderson, Cambridge Univ. Press, London.

871   Liljeblad, E., Karlsson, T., Raines, J. M., Slavin, J. A., Kullen, A., Sundberg, T. and Zurbuchen, T.

872   H. (2015). MESSENGER observations of the dayside low-latitude boundary layer in Mercury's

873   magnetosphere. J. Geophys. Res. Space Physics, 120, 8387–8400, doi:10.1002/2015JA021662.

874   Massetti, S., Orsini, S., Milillo, A., Mura, A., deAngelis, E., Lammer, H. and Wurz, P. (2003).

875   Mapping of the cusp plasma precipitation on the surface of Mercury. Icarus, 166, 229–237,

876   doi:10.1016/j.icarus.2003.08.005.

877   Muller, J., Simon, S., Wang, Y.-C., Motschmann, U., Heyner, D., Schu☐le, J., Ip, W.-H., Keindienst,

878   G. and Pringle, G. J. (2012). Origin of Mercury's double magnetopause: 3D hybrid simulation

879   with A.I.K.E.F. Icarus, 218, 666–687, doi:10.1016/j.icarus. 2011.12.028.

880   Ness, N. F., Behannon, K. W., Lepping, R. P., Whang, Y. C. and Schatten, K. H. (1974). Magnetic

881   field observations near Mercury: Preliminary results from Mariner 10. Science, 185,151–185.

40

882   Odstrcil, D., Riley, P. and Zhao, X. P. (2004). Numerical simulation of the 12 May 1997

883   interplanetary CME event. J. Geophys. Res., 109, A02116, doi:10.1029/2003JA010135.

884   Ogilvie, K. W., J. D. Scudder, V. M. Vasyliunas, R. E. Hartle, and G. L. Siscoe (1977) Observations

885   at the planet Mercury by the plasma electron experiment, Mariner 10, J. Geophys. Res., 82, 13,

886   1807-1824.

887   Paschmann, G., Papamastorakis, I., Baumjohann, W., Carlson, B. U., Lu□hr, H., Sckope, N. W. and

888   Sonnerup, O. (1986). The magnetopause for large magnetic shear: AMPTE/IRM observations. J.

889   Geophys. Res., 91, 11,099–11,115, doi:10.1029/JA091iA10p11099.

890   Pfleger, M., Lichtenegger, H. I. M., Wurtz, P., Lammer, H., Kallio, E., Alho, M., Mura, A.,

891   McKenna-Lawlor, S. and Martin-Fernandez, J. A. (2015). 3D-modeling of Mercury's solar wind

892   sputtered   surface-exosphere   environment.   Planet.   Space   Sci.,   115,   90–101,

893   doi:10.1016/j.pss.2015.04.016.

894   Poh, G., et al. (2016), MESSENGER observations of cusp plasma filaments at

895   Mercury, J. Geophys. Res. Space Physics, 121, 8260–8285, doi:10.1002/2016JA022552.

896   Raeder, J. (2006). Flux transfer events: 1. Generation mechanism for strong southward IMF. Ann.

897   Geophys., 24, 381–392, doi:10.5194/angeo-24–381-2006.

898   Raines, J. M., Gershman, D. J., Slavin, J. A., Zurbuchen, T. H., Korth, H., Anderson, B. J. and

899   Solomon, S. C. (2014). Structure and dynamics of Mercury's magnetospheric cusp:

900   MESSENGER measurements of protons and planetary ions. J. Geophys. Res. Space Physics,

901   119, 6587–6602, doi:10.1002/2014JA020120.

902   Raines, J. M., DiBraccio, G. A., Cassidy, T. A., Delcourt, D. C., Fujimoto, M., Jia, X., Mangano, V.,

903   Milillo, A., Sarantos, M., Slavin, J. A. and Wurz, P. (2015). Plasma sources in planetary

41

904   magnetospheres: Mercury. Space Sci. Rev., 192, 91–144, doi:10.1007/s11214-015–0193-4.

905   Ridley, A. J., Alfvén wings at Earth's magnetosphere under strong interplanetary magnetic fields.

906   Annales Geophysicae, European Geosciences Union, 2007, 25 (2), pp.533-542

907   Rijnbeek, R. P., Cowley, S. W. H., Southwood, D. J. and Russell, C. T. (1984). A survey of dayside

908   flux transfer events observed by ISEE-1 and ISEE-2 magnetometers. J. Geophys. Res., 89,

909   786–800, doi:10.1029/JA89iA02p00786.

910   Russell, C. T. and Elphic, R. C. (1978). Initial ISEE magnetometer results: Magnetopause

911   observations. Space Sci. Res., 22, 681–715, doi:10.1007/BF00212619.

912   Sarantos, M. and Slavin, J.A. (2009). On the possible formation of Alfven wings at Mercury during

913   encounter   with   coronal   mass   ejections.   Geophys.   Res.   Lett.   36,   L04107,

914   doi:10.1029/2008GL036747.

915   Siscoe, G. and Christopher, L. (1975). Variations in the solar wind stand-off distance at Mercury.

916   Geophys. Res. Lett., 2, 158–160, doi:10.1029/GL002i004p00158.

917   Shue, J. -H., J. K. Chao, H. C. Fu, C. T. Russell, P. Song, K. K. Khurana, and H. J. Singer (1997), A

918   new functional form to study the solar wind control of the magnetopause size and shape, Journal

919   of Geophysical Research, Volume 102, Issue A5, p. 9497-9512, doi:10.1029/97JA00196

920   Siscoe, G. and Christopher, L. (1975). Shue, J. -H., J. K. Chao, H. C. Fu, C. T. Russell, P. Song,

921   K. K. Khurana, and H. J. Singer, A new functional form to study the solar wind control of the

922   magnetopause size and shape Variations in the solar wind stand-off distance at Mercury.

923   Geophys. Res. Lett., 2, 158–160, doi:10.1029/GL002i004p00158.

924   Siscoe, G. and Christopher, L. (1975). Variations in the solar wind stand-off distance at Mercury.

925   Geophys. Res. Lett., 2, 158–160, doi:10.1029/GL002i004p00158.

926 Slavin, J. A., and R. E. Holzer (1979), The effect of erosion on the solar wind stand-off distance at

927 Mercury, J. Geophys. Res., 84, 2,076-2,082.

928 Slavin, J. A., R. C. Elphic, C. T. Russell, F. L. Scarf, J. H. Wolfe, J. D. Mihalov, D. S. Intriligator, L.

929 H. Brace, H. A. Taylor, Jr., and R. E. Daniell, Jr. (1980), The solar wind interaction with Venus:

930 Pioneer Venus Observations of bow shock location and structure, J. Geophys. Res., 85, 7,625

931 Slavin, J. A., and R. E. Holzer (1981), Solar wind flow about the terrestrial planets, 1. Modeling

932 bow shock position and shape, J. Gophys. Res., 86, A13, 11,401-11,418.

933 Slavin, J. A., E. J. Smith, D. G. Sibeck, D. N. Baker, R. D. Zwickl, and S.-I. Akasofu (1985), An

934 ISEE-3 study of average and substorm conditions in the distant magnetotail, J. Geophys. Res.,

935 90, A11,10,875–10,895.

936 Slavin, J.A., D.H. Fairfield, R.P. Lepping, A. Szabo, M.J. Reiner, M. Kaiser, C.J. Owen, T. Phan, R.

937 Lin, S. Kokubun, T. Mukai, T. Yamamoto, H. Singer, S. Romanov, J. Buechner, T. Iyemori, and

938 G. Rostoker (1997), WIND, GEOTAIL and GOES 9 observations of magnetic field

939 dipolarization and bursty bulk flows in the near-tail, Geophys. Res. Lett., 24, 971

940 Slavin, J. A., B. J. Anderson, T. H. Zurbuchen, D. N. Baker, S. M. Krimigis, M. H. Acuña, M.

941 Benna, S. A. Boardsen, G. Gloeckler, R. E. Gold, G. C. Ho, H. Korth, R. L. McNutt, Jr., J. M.

942 Raines, M. Sarantos, D. Schriver, S. C. Solomon, and P. Trávníček (2009), MESSENGER

943 observations of Mercury's magnetosphere during northward IMF, Geophys. Res. Lett., 36,

944 L02101, doi:10.1029/2008GL036158

945 Slavin, J. A., B. J. Anderson, D. N. Baker, M. Benna, S. A. Boardsen, G. Gloeckler, R. E. Gold, G.

946 C. Ho, H. Korth, S. M. Krimigis, R. L. McNutt, Jr., L. R. Nittler, J. M. Raines, M. Sarantos, D.

947 Schriver, S. C. Solomon, R. D. Starr, P. M. Trávníček, T. H. Zurbuchen (2010a), MESSENGER

948   observations of extreme loading and unloading of Mercury's magnetic tail, Science, 329, 665-

949   668.

950   Slavin, J. A., R. P. Lepping, C. –C. Wu, B. J. Anderson, D. N. Baker, M. Benna, S. A. Boardsen, R.

951   M. Killen, H. Korth, S. M. Krimigis, W. E. McClintock, R. L. McNutt Jr., M. Sarantos, D.

952   Schriver, S. C. Solomon, P. Travnicek, and T. H. Zurbuchen (2010b), MESSENGER

953   observations of large flux transfer events at Mercury, Geophys. Res. Lett., 37, L02105,

954   doi:10.1029/2009GL041485.

955   Slavin, J. A., S. M. Imber, S. A. Boardsen, G. A. DiBraccio, T. Sundberg, M. Sarantos, T. Nieves-

956   Chinchilla, A. Szabo, B. J. Anderson, H. Korth, T. H. Zurbuchen, J. M. Raine C. L. Johnson, R.

957   M. Winslow, R. M. Killen, R. L. McNutt, Jr., and S. C. Solomon (2012), MESSENGER

958   Observations of a Flux Transfer Shower at Mercury, J. Geophys. Res., 117, A00M06,

959   doi:10.1029/2012JA017926.

960   Slavin, J. A., G. A. DiBraccio, D. J. Gershman, S. Imber, G. K. Poh, J. Raines, T. H. Zurbuchen, X.

961   Jia, D. N. Baker, S. A. Boardsen, T. Sundberg, A. Masters, C. L. Johnson, R. M. Winslow, B. J.

962   Anderson, H. Korth, G. Ho, S. M. Krimigis, R. L. McNutt, Jr, and S. C. Solomon (2014),

963   MESSENGER Observations of Mercury's Dayside Magnetosphere Under Extreme Solar Wind

964   Conditions, J. Geophys. Res. Space Physics, 119, doi:10.1002/2014JA020319.

965   Slavin, J. A., D. N. Baker, D. J. Gershman, G. Ho, S. M. Imber, S. M. Krimigis, and T. Sundberg

966   (2019), Mercury's Dynamic Magnetosphere, in Mercury: The view after MESSENGER, eds. S.

967   C., L. R. Nittler, and B. J. Anderson, Cambridge Univ. Press, London, ISBN: 978-1107154452.

968   Smith, D. E., Zuber, M. T., Phillips, R. J., Solomon, S. C., Hauck, S. A., II, Lemoine, F. G.,

969   Mazarico, E., Neumann, G. A., Peale, S. J., Margot, J.-L., Johnson, C. L., Torrence, M. H.,

44

970   Perry, M. E., Rowlands, D. D., Goossens, S., Head, J. W. and Taylor, A. H. (2012). Gravity

971   field and internal structure of Mercury from MESSENGER. Science, 336, 214–217.

972   Solomon, S. C., McNutt, R. L., Jr., Gold, R. E. and Domingue, D. L. (2007). MESSENGER

973   mission overview. Space Sci. Rev., 131, 3–39, doi:10.1007/s11214-007–9247-6.

974   Sonnerup, B. U. Ö, Papmastorakis, I., Paschmann, G. and Lu☐hr, H., (1990). The magnetopause

975   for large magnetic shear: Analysis of convection electric fields from AMPTE/IRM. J.

976   Geophys. Res., 95, 10,541–10,557, doi:10.1029/JA095iA07p10541.

977   Spreiter, J. R., Summers, A. L. and Alksne, A. Y. (1966). Hydromagnetic flow around the

978   magnetosphere. Planet. Space Sci., 14, 223–253, doi:10.1016/0032–0633(66)90124–3.

979   Suess, S. T. and Goldstein, B. E. (1979). Compression of the Hermaean magnetosphere by the

980   solar wind. J. Geophys. Res., 84, 3306–3312, doi:10.1029/JA084iA07p03306.

981   Tanskanen, E. I. (2009). A comprehensive high-throughput analysis of substorms observed by

982   IMAGE magnetometer network: Years 1993–2003 examined. J. Geophys. Res., 114,

983   A05204, doi:10.1029/2008JA013682.

984   Toth, G. and Odstrcil, D. (1996). Comparison of some flux corrected transport and total variation

985   diminishing numerical schemes for hydrodynamic and magnetohydrodynamic problems. J.

986   Comput. Phys., 128, 82–100.

987   Trávníček, P. M., Hellinger, P., Schriver, D., Herčík, D., Slavin, J. A. and Anderson, B. J.

988   (2009).

989   Kinetic instabilities in Mercury's magnetosphere: Three-dimensional simulation results.

990   Geophys. Res. Lett., 36, L07104, doi:10.1029/2008GL036630.

991   Trávníček, P. M., Schriver, D., Hellinger, P., Herčík, D., Anderson, B. J., Sarantos, M. and

992   Slavin, J. A. (2010). Mercury's magnetosphere–solar wind interaction for northward and

993   southward

994   interplanetary   magnetic   field: Hybrid   simulations.   Icarus,   209,   11–22,

995   doi:10.1016/j.icarus.2010.01.008.

996   Trenchi, L., Marcucci, M. F., Rème, H., Carr, C. M. and Cao, J. B. (2011). TC-1 observations of

997   a flux rope: Generation by multiple X line reconnection. J. Geophys. Res., 116, A05202,

998   doi:10.1029/2010JA015986.

999   Varela, J., Pantellini, F. and Moncuquet, M. (2015). The effect of interplanetary magnetic field

1000   orientation on the solar wind flux impacting Mercury's surface. Planet. Space Sci., 119, 264–

1001   269, doi:10.1016/l.pss.2015.10.004.

1002   Wang, Y. C., Motschmann, U., Mü☐ ller, J. and Ip, W. H. (2010). A hybrid simulation of

1003   Mercury's magnetosphere for the MESSENGER encounters in year 2008. Icarus, 209, 46–

1004   52. et al., 2010

1005   Webster, J. M., Burch, J. L., Reiff, P. H., Daou, A. G., Genestreti, K. J., Graham, D. B., et al. (2018).

1006   Magnetospheric Multiscale dayside reconnection electron diffusion region events. Journal of

1007   Geophysical Research: Space Physics, 123, 4858–4878. https:// doi.org/10.1029/2018JA025245

1008   Winslow, R. M., Johnson, C. L., Anderson, B. J., Korth, H., Slavin, J. A., Purucker, M. E. and

1009   Solomon, S. C. (2012). Observations of Mercury's northern cusp region with

1010   MESSENGER's   Magnetometer.   Geophys.   Res.   Lett.,   39,   L08112,

1011   doi:10.1029/2012GL051472.

1012 Winslow, R. M., Anderson, B. J., Johnson, C. L., Slavin, J. A., Korth, H., Purucker, M. E.,

1013 Baker,

1014 D. N. and Solomon, S. C. (2013). Mercury's magnetopause and bow shock from

1015 MESSENGER observations. J. Geophys. Res. Space Physics, 118, 2213–2227,

1016 doi:10.1002/jgra.50237.

1017 Winslow, R. M., Winslow, R. M., N. Lugaz, L. C. Philpott, N. A. Schwadron, C. J. Farrugia, B.

1018 J. Anderson, and C. W. Smith (2015), Interplanetary coronal mass ejections from

1019 MESSENGER orbital observations at Mercury, J. Geophys. Res. Space Physics, 120, 6101–

1020 6118,

1021 doi:10.1002/2015JA021200.

1022 Winslow, R. M., N. Lugaz, C. J. Farrugia1, C. L. Johnson, B. J. Anderson, C. S. Paty, N. A.

1023 Schwadron, L. Philpott, M. Al Asad, First observations of an ICME compressing

1024 Mercury'sdayside magnetosphere to the surface, arXiv:1903.00577v1 (2019).

1025 Zhong, J., Wan, W. X., Slavin, J. A., Wei, Y., Lin, R. L., Chai, L. H., Raines, J. M., Rong, Z. J.

1026 and Han, X. H. (2015a). Mercury's three-dimensional asymmetric magnetopause. J.

1027 Geophys. Res. Space Physics, 120, 7658–7671, doi:10.1002/2015JA021425.

1028 Zhong, J., Wan, W. X., Wei, Y., Slavin, J. A., Raines, J. M., Rong, Z. J., Chai, L. H. and Han, X.

1029 H. (2015b). Compressibility of Mercury's dayside magnetosphere. Geophys. Res. Lett., 42,

1030 10,135–10,139, doi:10.1002/2015GL067063.

1031 Zong, Q.-G., Fritz, T. A., Spence, H., Zhang, H., Huang, Z. Y., Pu, Z. Y., Glassmeier, K.-H.,

1032 Korth, A., Daly, P. W., Balogh, A. and Reme, H. (2005). Plasmoid in the high latitude

47

1033   boundary/cusp   region   observed   by   Cluster,   2014andGeophys.   Res.   Lett.,32,

1034   L01101,doi:10.1029/2004GL020960 .

1035

Table 1. Magnetopause Analysis Results

Year	DOY	UTC	Type[a]	$X'_{MSM}\ Y'_{MSM}\ Z'_{MSM}\ (R_M)$	$\mathbf{B}_N/|\mathbf{B}_N|$	B_N (nT)	α[b]	P_{SW} (nPa)	$R_{SS}\ (R_M)$
2011	288	14:39:00	DDM	(0.13, 0.05, 0.96)	(0.80, 0.38, 0.46)	51.87	0.12	142.4	0.66
2013	335	01:34:30	DDM	(0.13, 0.08, 0.93)	(0.68, 0.01, 0.74)	68.60	0.16	181.9	0.64
2014	44	10:00:30	DDM	(0.09, 0.24, 0.88)	(0.63, -0.20, 0.75)	83.65	0.17	288.5	0.61
2015	84	00:41:45	DDM	(0.17, -0.03, 0.89)	(0.78, 0.08, 0.63)	165.19	0.29	233.0	0.66

[a]Disappearing Dayside Magnetosphere (DDM)   [b]Dimensional reconnection rate $\alpha = B_N/B_{MP}$

1036

1037

1038   Figure 1. The (a) Increases in solar wind pressure drive induction currents (green loops) at the

1039   top of Mercury's large iron core. The sense of these currents is to oppose the compression of the

1040   intrinsic magnetic field (yellow) by generating additional magnetic flux (green field lines) that,

1041   when added to the intrinsic flux, acts to balance the increased solar wind pressure. (b) Magnetic

1042   reconnection between the interplanetary magnetic field and the intrinsic planetary magnetic field

1043   opposes the effectiveness of induction by removing magnetic flux from the dayside

1044   magnetosphere and transporting it to the tail (adapted from Slavin et al., 2014).

1045

1046   Figure 2. Every other MESSENGER orbit for its four-year mission have been plotted in solar

1047   wind aberrated, cylindrical MSO coordinates. The mean bow shock and magnetopause from the

1048   axisymmetric conic surfaces determined by Winslow et al. (2013) are displayed. Note the clear

1049   signature of the change in apoapsis altitude early in the mission and the dense coverage of the

1050   near-Mercury magnetosheath and magnetosphere (see discussion in Slavin et al., 2007; 2019)

1051

1052   Figure 3. Full resolution (20/sec) MAG measurements in MSM coordinates for 15 October 2011.

1053   Probable identifications for the arrival of an interplanetary shock and a coronal mass ejection are

1054   indicated. The peak magnetic fields for the two periapsis passes are displayed along with the

1055   altitudes where they were recorded.

1056

1057   Figure 4. ENLIL-WSA+Cone models of (a) solar wind radial speed (V_r) and (b) the product of

1058   solar wind density (n) and the square of distance (r) from the Sun in AU for 15 October 2011 at

49

1059   21:00 UTC. Coronal mass ejections identified in the SOHO and STEREO observations are

1060   enclosed by solid black lines. The center of a coronal mass ejection impacted Mercury and its

1061   magnetosphere (yellow circle). The locations of Earth, Venus, and Mercury are all indicated by

1062   small colored dots. The inner domain of the model (where WSA is utilized) is denoted by the

1063   central white circle. (c–d) Magnetic field B_z and total intensity (B) measurements (sampled at a

1064   rate of 20 sec-1). The smoothed magnetic field data shown with the red traces.

1065

1066   Figure 5. MESSENGER measurements of B_z and B magnitude (20 s-1) in in MSM coordinates

1067   on 15 October 2011and 1 December 2013. The interval presented covers the upstream

1068   interplanetary medium, the dayside pass from the low-latitude bow shock (BS) to the high

1069   latitude magnetopause (MP) crossings and, finally, the near-tail. Large amplitude, high

1070   frequency fluctuations are observed from the bow shock through to the magnetopause where

1071   they quickly decrease in amplitude.

1072   Figure 6. MESSENGER measurements of B_z and B magnitude (20 sec-1) in in MSO

1073   coordinates on 13 February 2014 and 25 March 2015. The interval presented covers the upstream

1074   interplanetary medium, the dayside pass from the low-latitude bow shock (BS) to the high

1075   latitude magnetopause (MP) crossings and, finally, the near-tail. Note that the final DDM event

1076   in the bottom panels is the only descending pass wherein MESSENGER passed from the high-

1077   latitude tail, through the magnetopause and then ended the dayside pass by exiting through the

1078   bow shock at low latitudes. As with the other DDM evens large amplitude, high frequency

1079   fluctuations are observed throughout these dayside passes.

1080

50

1081   **Figure 7.** Close-up views of the FIPS plasma measurements for each of the 3 DDM dayside

1082   passes. The FIPS H^+ E/Q spectra (cm^{-2} s^{-1} sr^{-1} keV^{-1}), H^+ observed density (cm^{-3}), He^+, He^{++}, O+

1083   and Na^+ observed densities (cm^{-3}), and B-total (nT) are shown in panels a-d for the 15 October

1084   2011 events, in panels e – h for 1 December 2013, and in panels i – l for 13 February 2014.

1085   Figure 8. Projections of MESSENGER's trajectory into the aberrated MSO a) Z'-X', b) Y'-X'

1086   and c) Z'-X' planes. The background magnetospheric magnetic field lines are from an MHD

1087   simulation [Jia et al., 2015]. The intervals over which the spacecraft was in the magnetosheath is

1088   shown in red while the magnetospheric traversals are shown in blue. Note: arrows indicate the

1089   direction of MESSENGER's motion.

1090

1091   Figure 9. The rates at which FTEs are observed for each of the DDM passes are displayed in

1092   panels a, c, e and g in bins of 30 sec duration. For each of the DDM passes red arrows mark the

1093   occurrence of individual FTEs against a plot of B-total in panels b, d, f, and h.

1094

1095   **Figure 10.** Histograms of a) FTE radius and b) FTE flux content for total of 438 FTEs identified

1096   and modeled by fitting to a force-free flux rope model (see Akhavan-Tafti et al, 2018).

1097

1098   Figure 11. MESSENGER MAG measurements (20 sec^{-1}) in MSM coordinates are displayed

1099   across the high-latitude magnetopause crossings for the 15 October 2011 and 01 December 2013

1100   disappearing dayside magnetosphere events. The smoothed magnetic field data shown with the

51

1101   red traces were created by performing a boxcar averaging on the magnetic field data using a 40

1102   sec window and used for minimum variance analysis. Vertical dashed lines mark the intervals

1103   used for MVA analysis and the minimum, intermediate and maximum Eigenvectors are listed in

1104   panels d and h.

1105   Figure 12. MESSENGER MAG measurements (20 sec-1) in MSM coordinates are displayed

1106   across the high-latitude magnetopause crossings for the 13 February 2014 and 25 March 2015

1107   disappearing dayside magnetosphere events. The smoothed magnetic field data shown with the

1108   red traces were created by performing a boxcar averaging on the magnetic field data using a 40

1109   sec window and used for minimum variance analysis. Vertical dashed lines mark the intervals

1110   used for MVA analysis and the minimum, intermediate and maximum Eigenvectors are listed in

1111   panels d and h.

1112

1113   Figure 13. The The locations of the bow shock (red marks) and magnetopause (blue marks)

1114   observed during the DDM passes are plotted in cylindrical solar wind aberrated MSM

1115   coordinates. Shue et al. (1997) boundary surfaces have been fit to the bow shock and

1116   magnetopause crossings and displayed in red and blue, respectively. For comparison the surface

1117   of Mercury and the much higher altitude mean surface determined by Winslow et al. (2013) are

1118   also displayed in gray.

1119

1120   Figure 14. The extrapolated stand-off distance of the nose of the magnetopause, R_{SS}, is plotted

1121   against the upstream solar wind dynamic pressure, Psw, for each of the 8 highly compressed

1122   dayside magnetosphere (HCM) and 4 disappearing dayside magnetosphere (DDM) intervals..

1123   The individual magnetopause crossings are displayed as square symbols with the size of box

1124   proportional to the dimensionless reconnection rate. A Chapman-Ferraro (CF) sixth-root of Psw

1125   curve intersecting the mean 10 - 15 nPa stand-off distance determined by Winslow et al. (2013)

1126   is the lower dashed line. The upper dashed line (black) is a theoretical model of the compression

1127   of Mercury's dayside magnetosphere by Glassmeier et al. (2007) that includes the effects of

1128   induction in Mercury's interior.

1129

53

1130   Figure 15. The primary features of the disappearing dayside magnetosphere events are illustrated

1131   with the magnetic field lines due to the core dynamo and the induction currents on the core

1132   surface, are shown in yellow and green, respectively. The bow shock is very close to the planet

1133   presumably due to solar wind impact and absorption. Large numbers of FTE-type flux ropes are

1134   observed and an unknown fraction of closed field lines are compressed into the crust by the high

1135   solar wind pressure.

1136

54
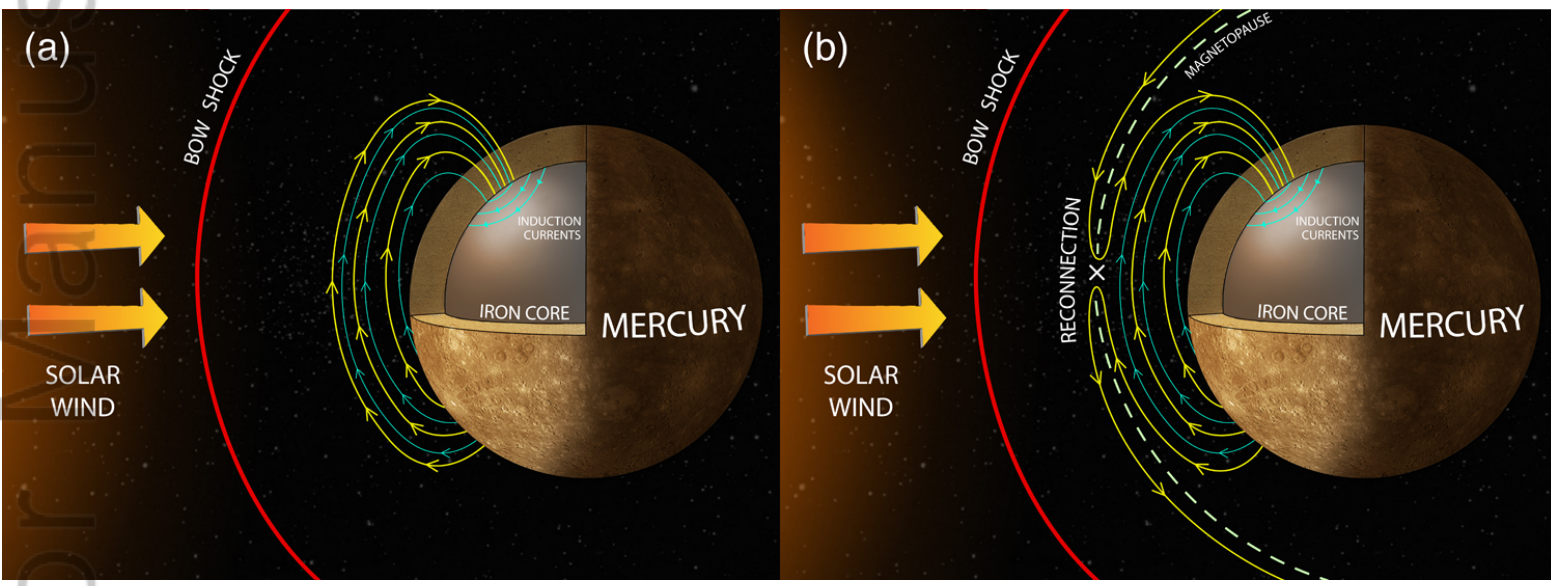
2019JA026892-f01-z-.jpg
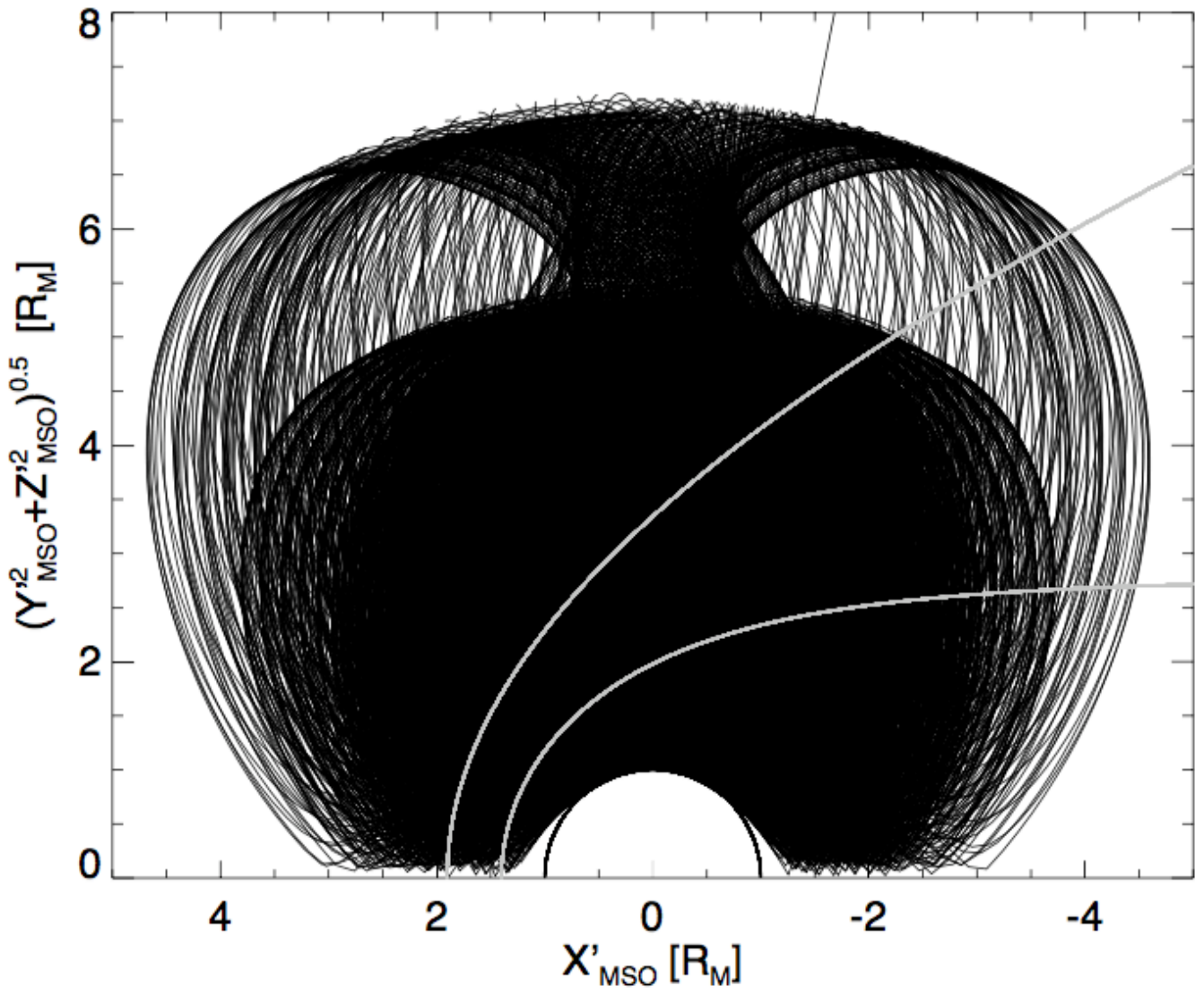
2019JA026892-f02-z-.png

2011 DOY 288 (10/15)
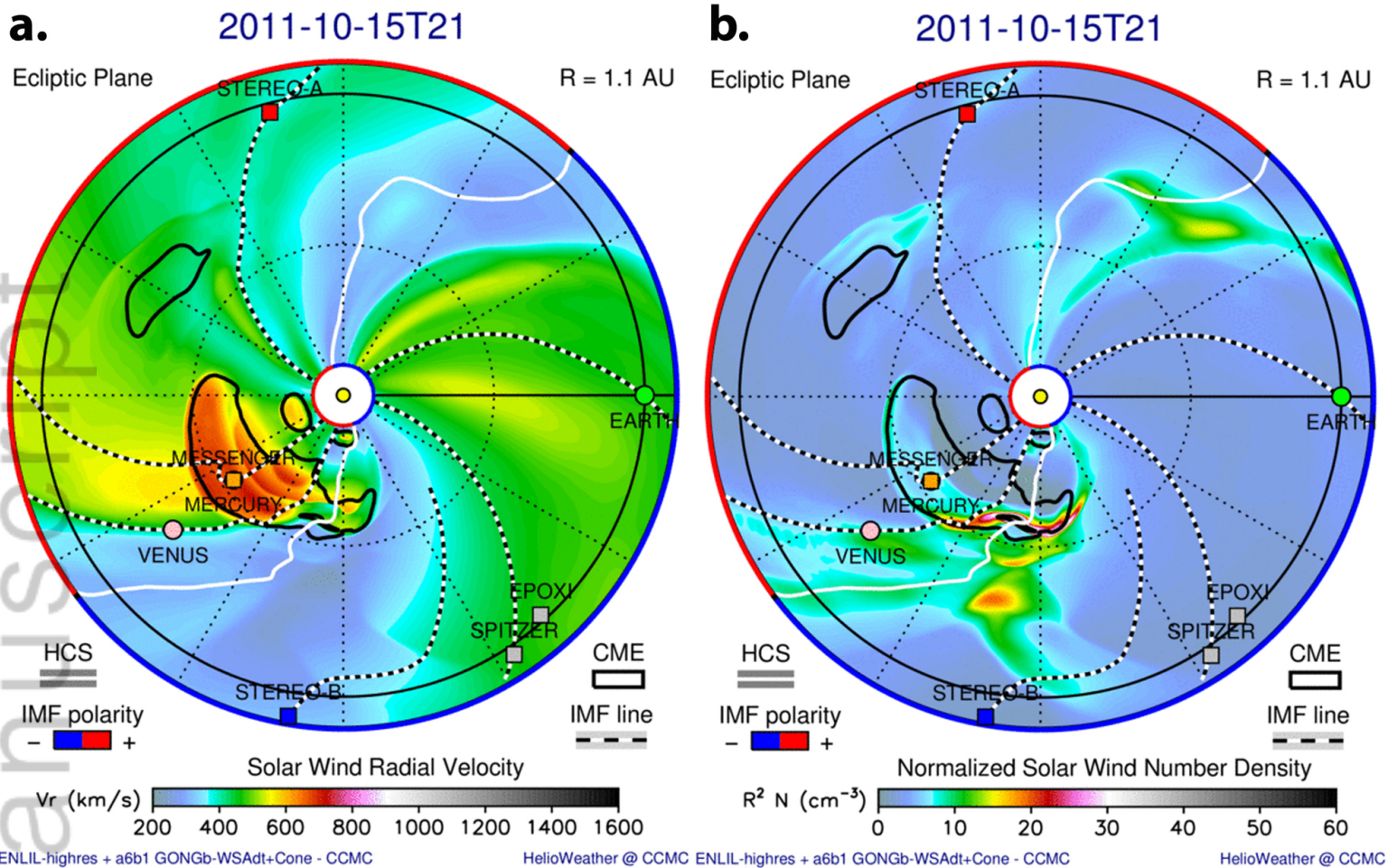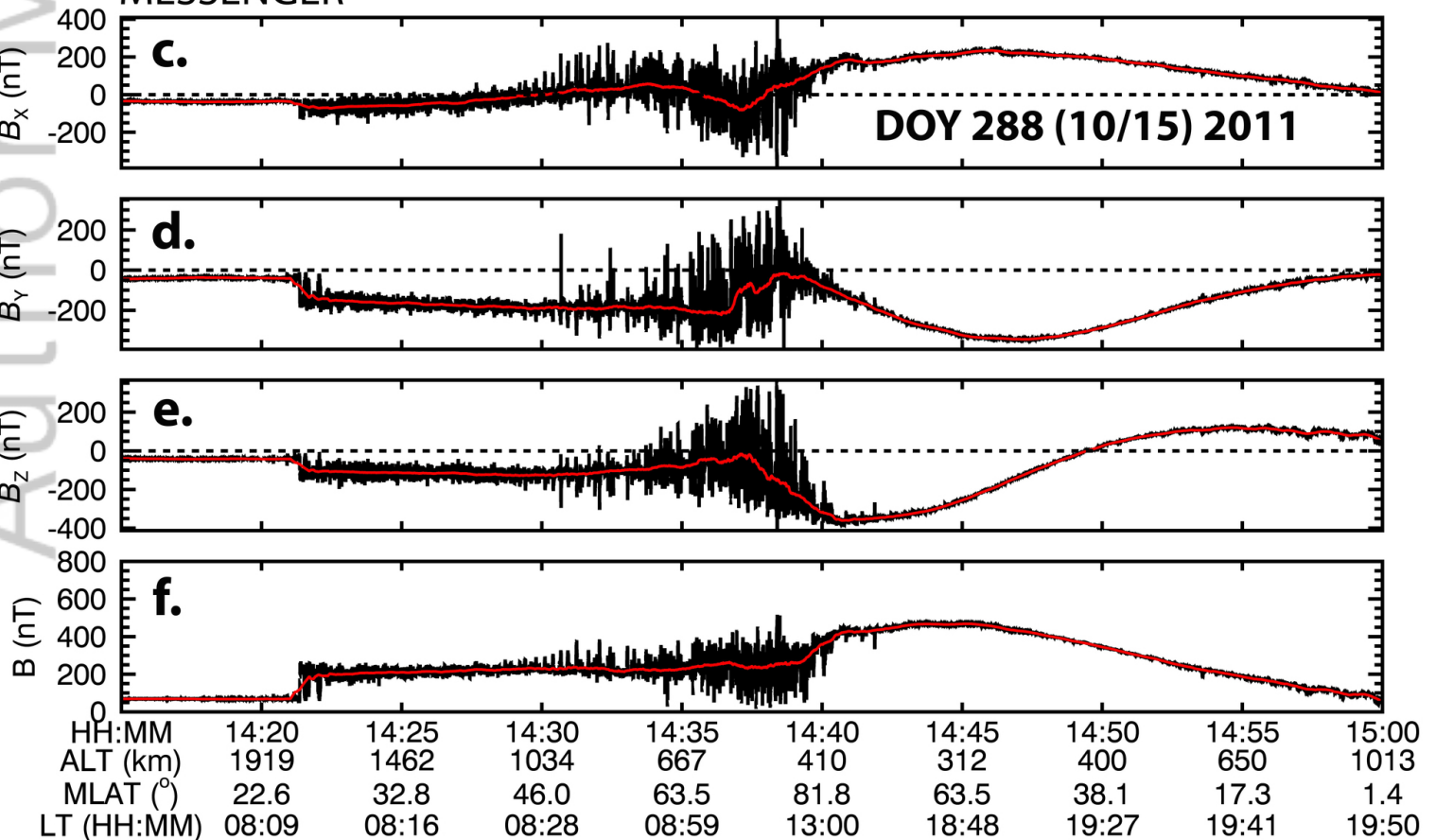
B_{max} = 410 nT
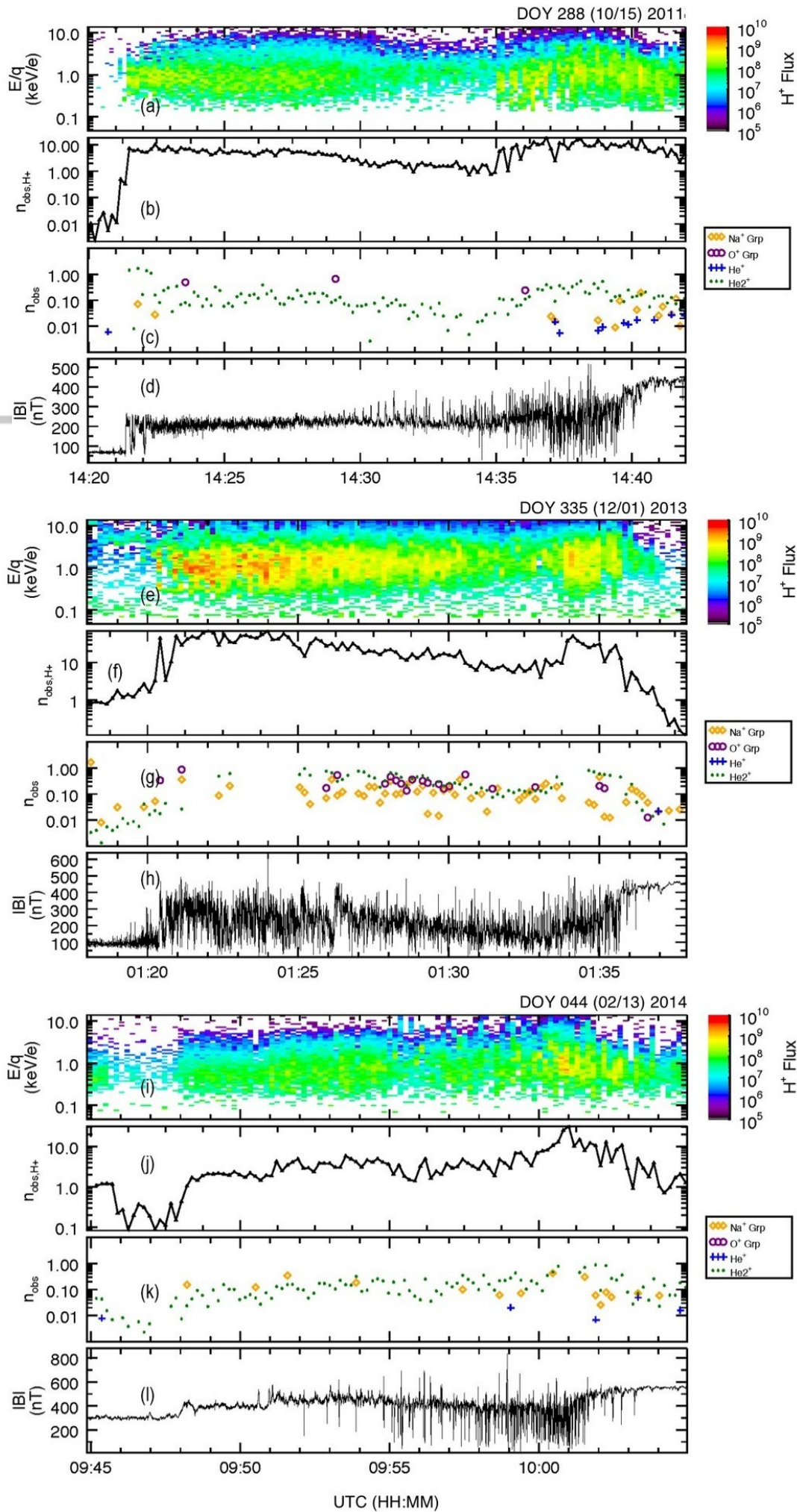Alt = 330 km

B_{max} = 470 nT
Alt = 320 km

IP SH

CME

2019JA026892-f03-z-.png

2019JA026892-f04-z-.jpg

MESSENGER

MESSENGER

a. DOY 044 (02/13) 2014

B_Z (nT)

600
400
200
0
-200
-400

MP

b.

1000
800
600
400
200

BS

HH:MM	09:35	09:40	09:45	09:50	09:55	10:00	10:05	10:10	10:15
ALT (km)	1827	1401	999	648	391	276	332	543	866
MLAT (°)	-17.0	-7.6	4.4	20.0	40.4	65.6	81.4	60.3	41.6
LT (HH:MM)	14:18	14:22	14:27	14:35	14:49	15:29	22:24	01:29	01:54

c. DOY 084 (03/25) 2015

B_Z (nT)

200
0
-200
-400
-600

MP

d.

1000
800
600
400
200
0

BS

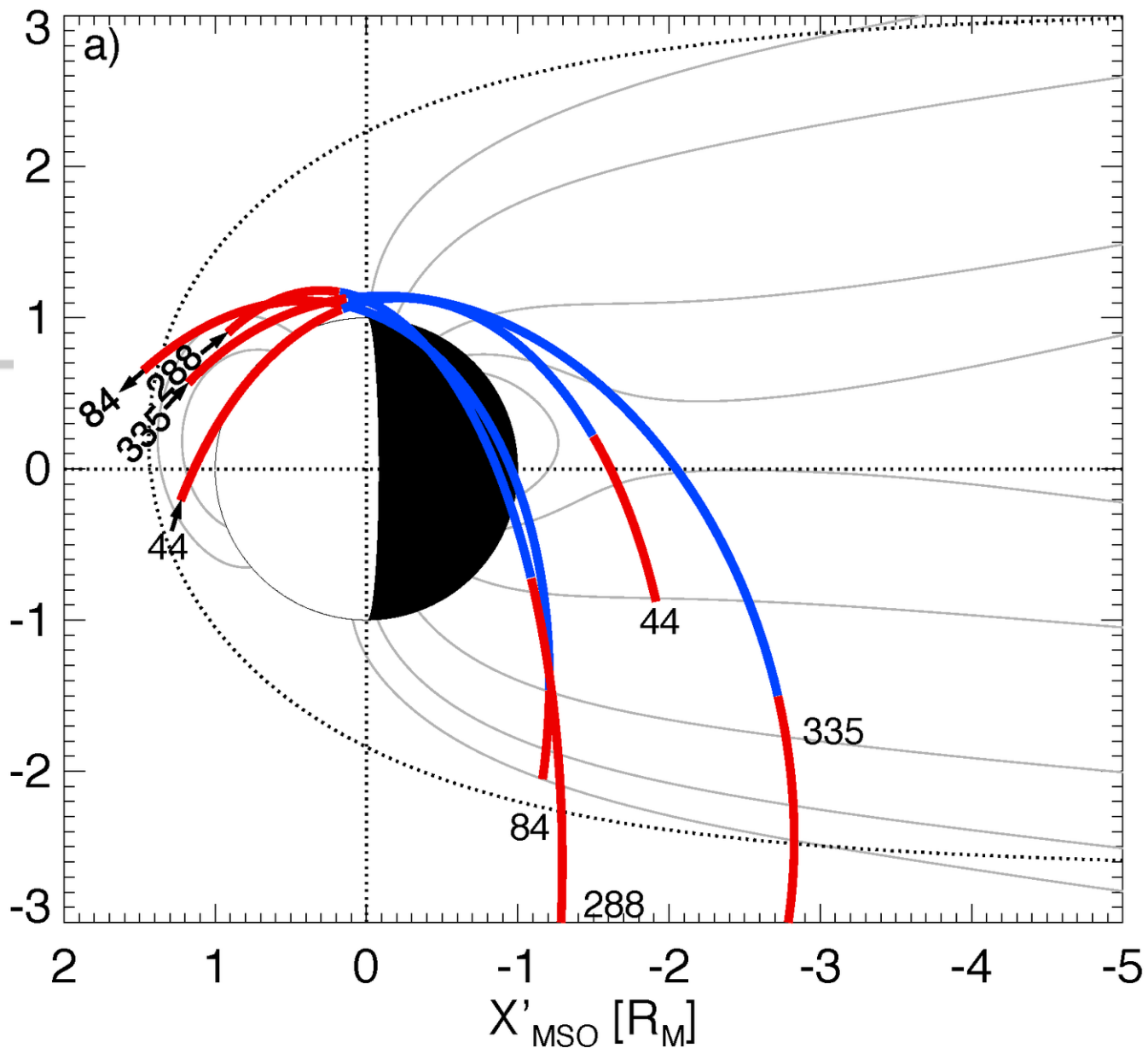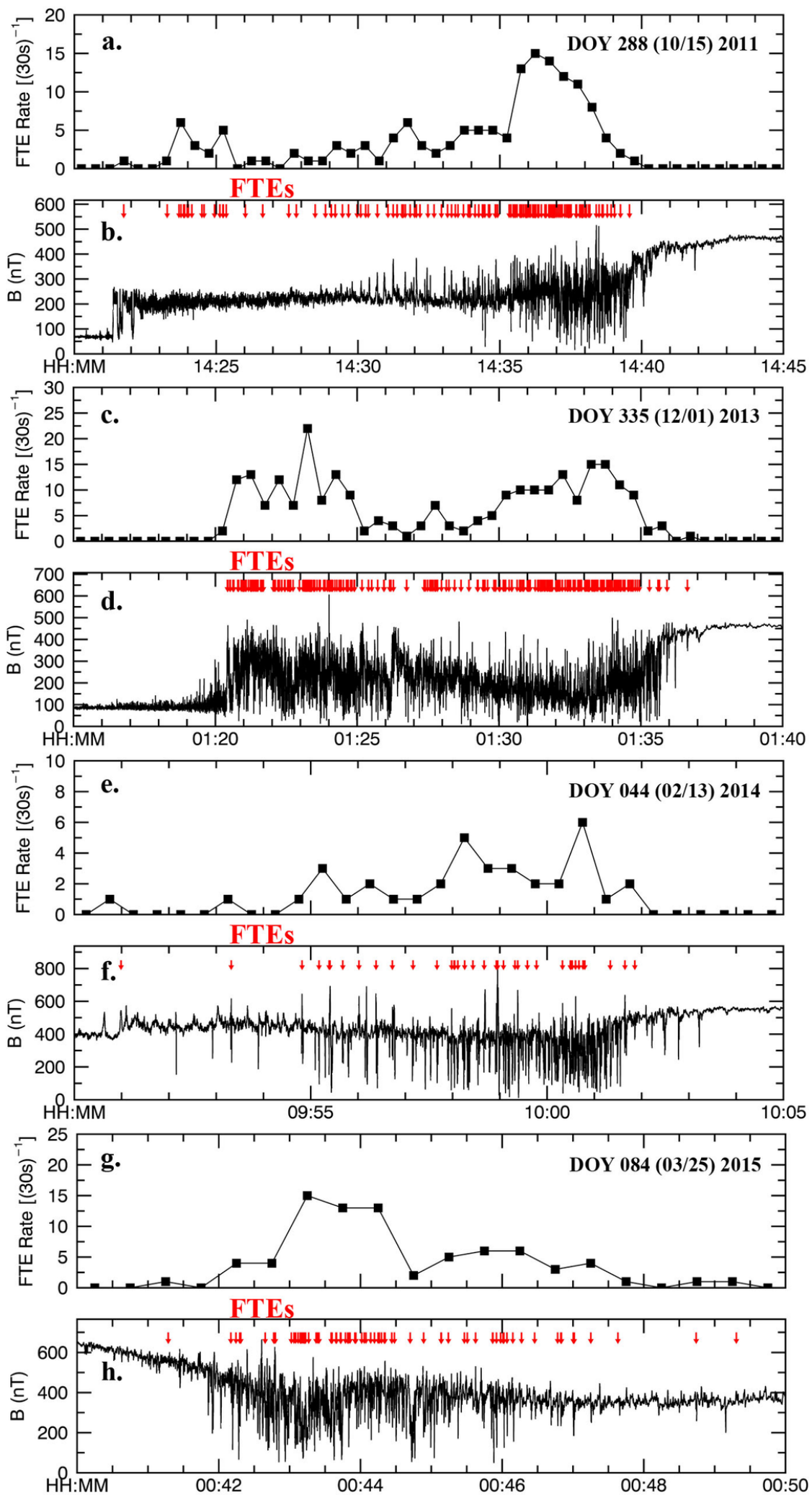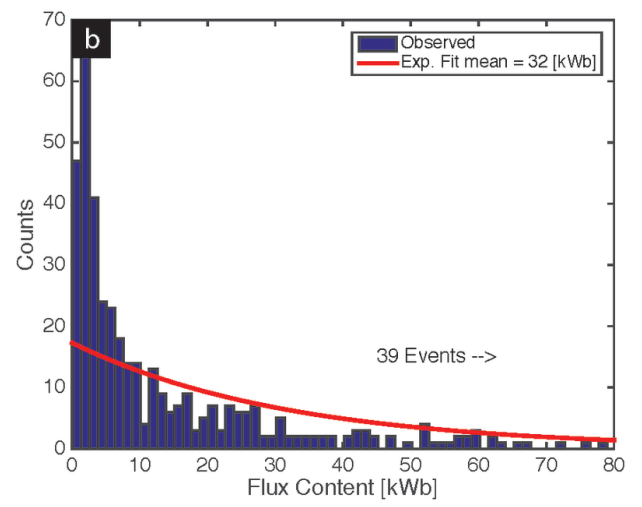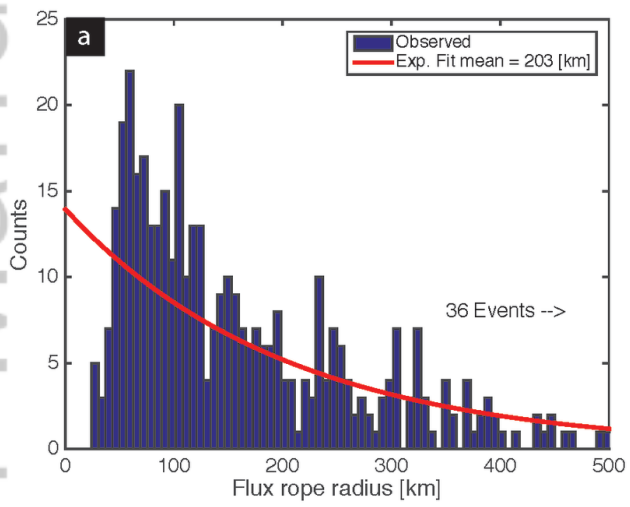| HH:MM	00:35	00:40	00:45	00:50	00:55	01:00	01:05	01:10	01:15
ALT (km)	28	146	442	847	1303	1776	2249	2712	3160
MLAT (°)	52.7	80.6	66.3	47.7	34.0	23.8	15.9	9.5	4.2
LT (HH:MM)	03:04	06:24	13:00	13:41	13:54	14:02	14:06	14:10	14:13
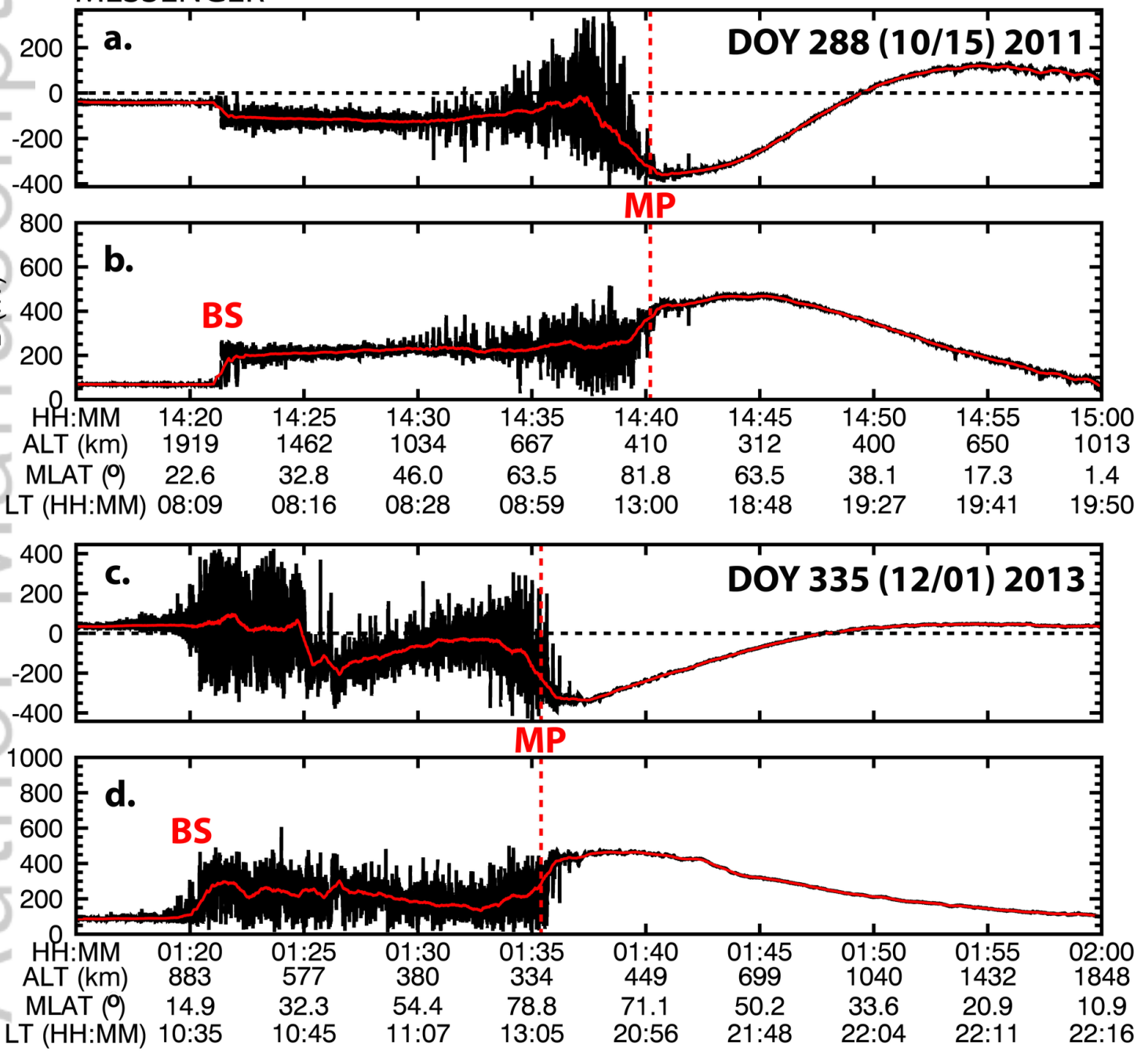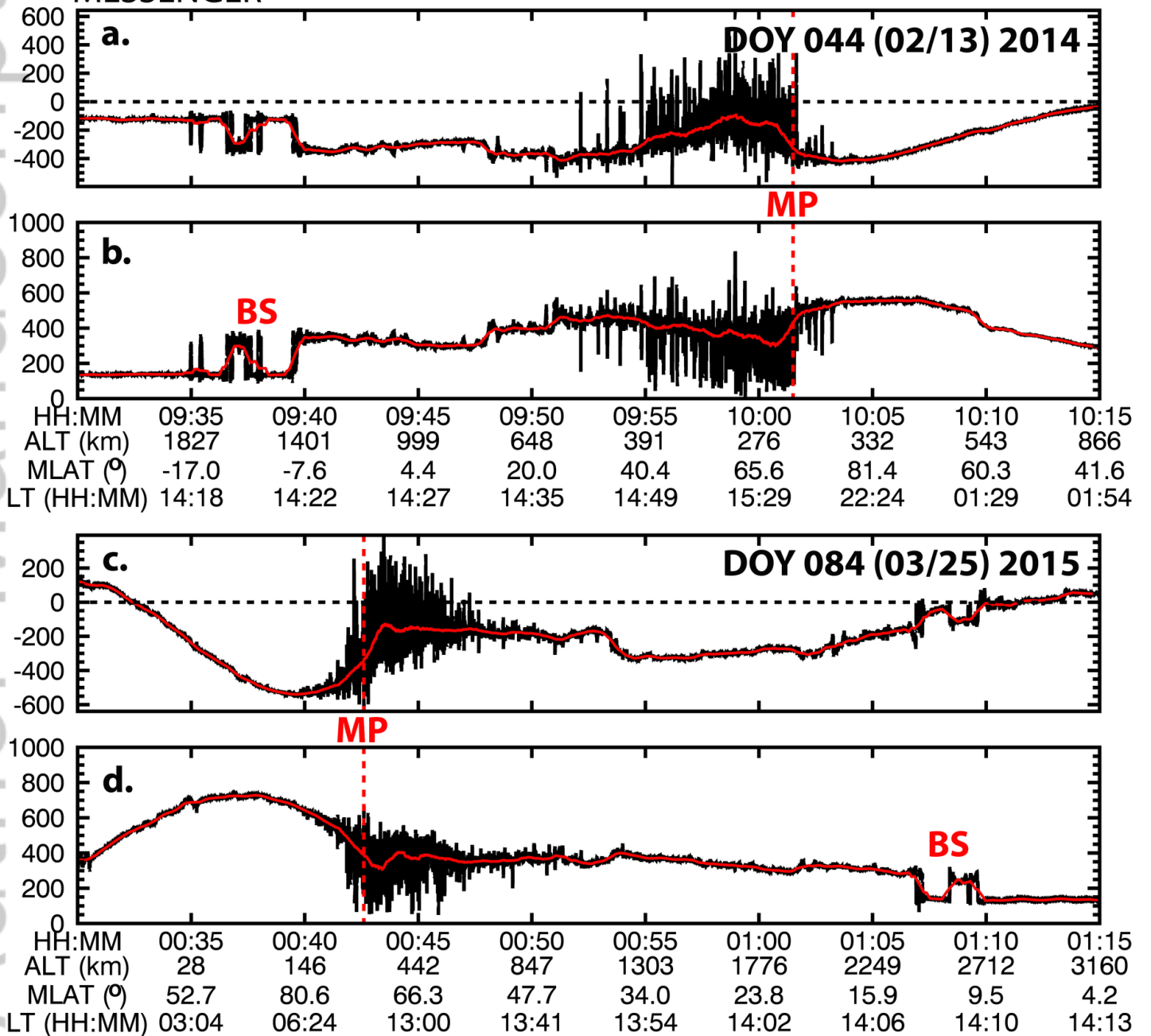
2019JA026892-f06-z-.tif

2019JA026892-f07-z-.jpg
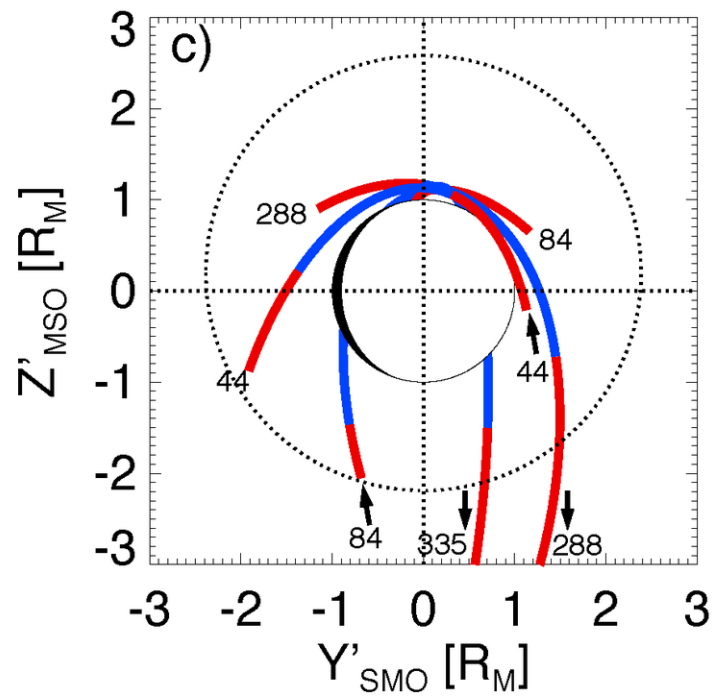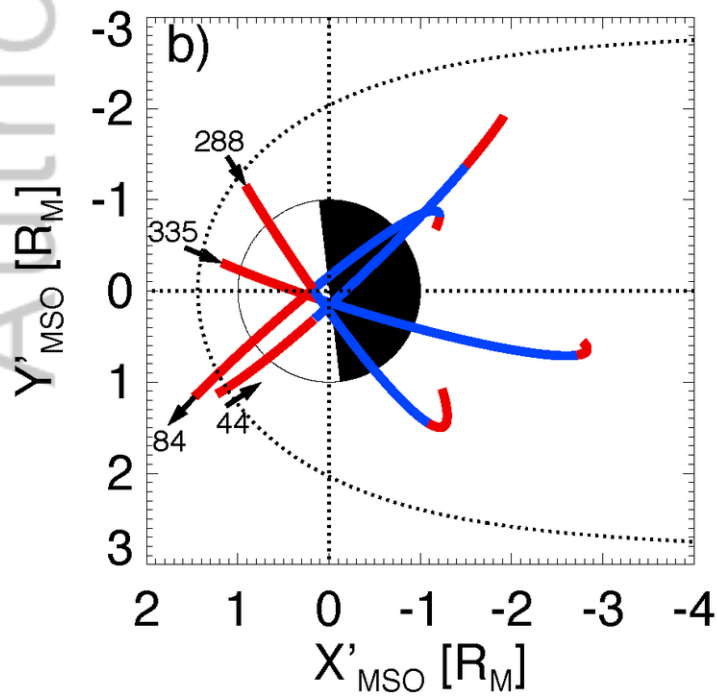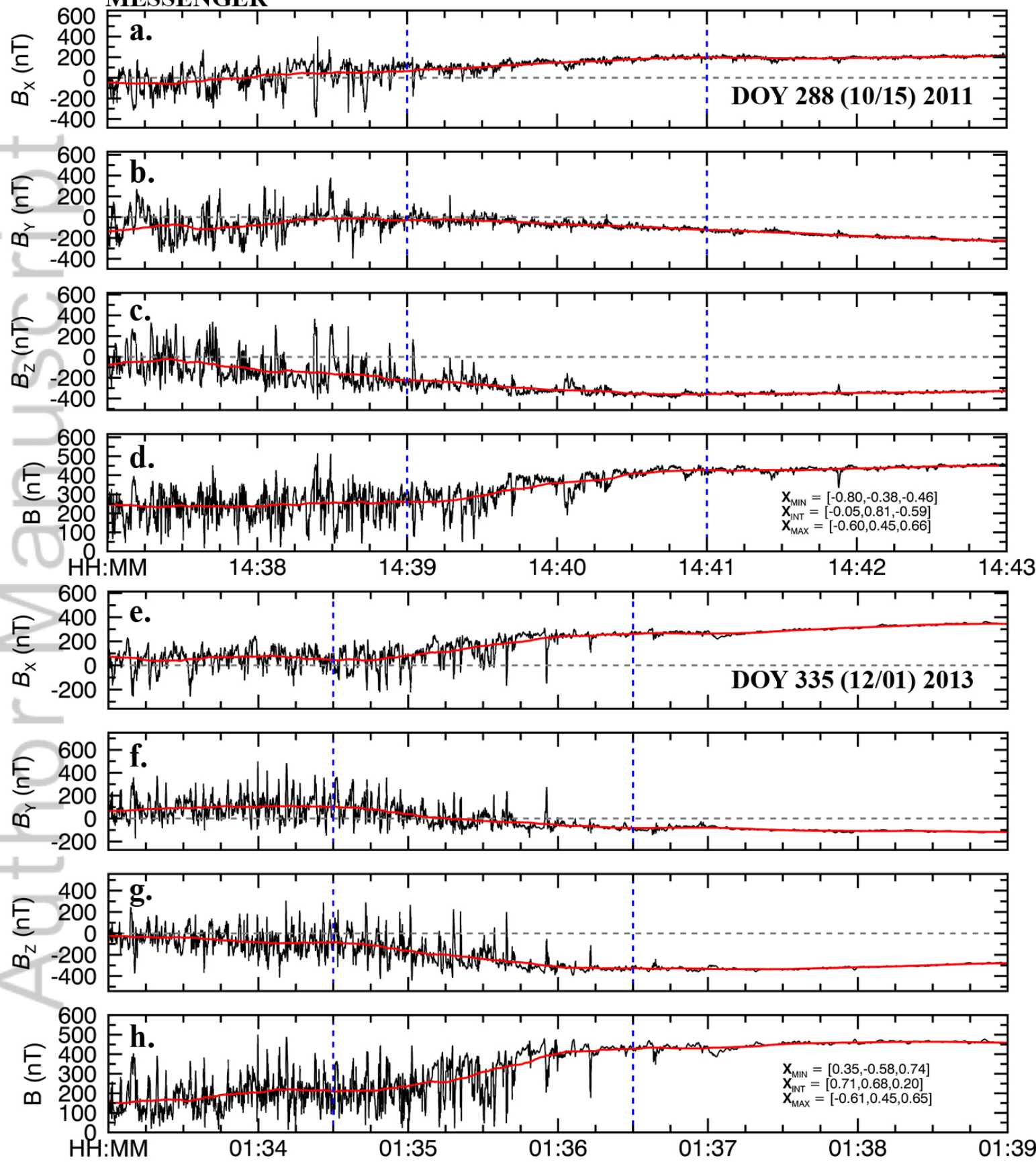
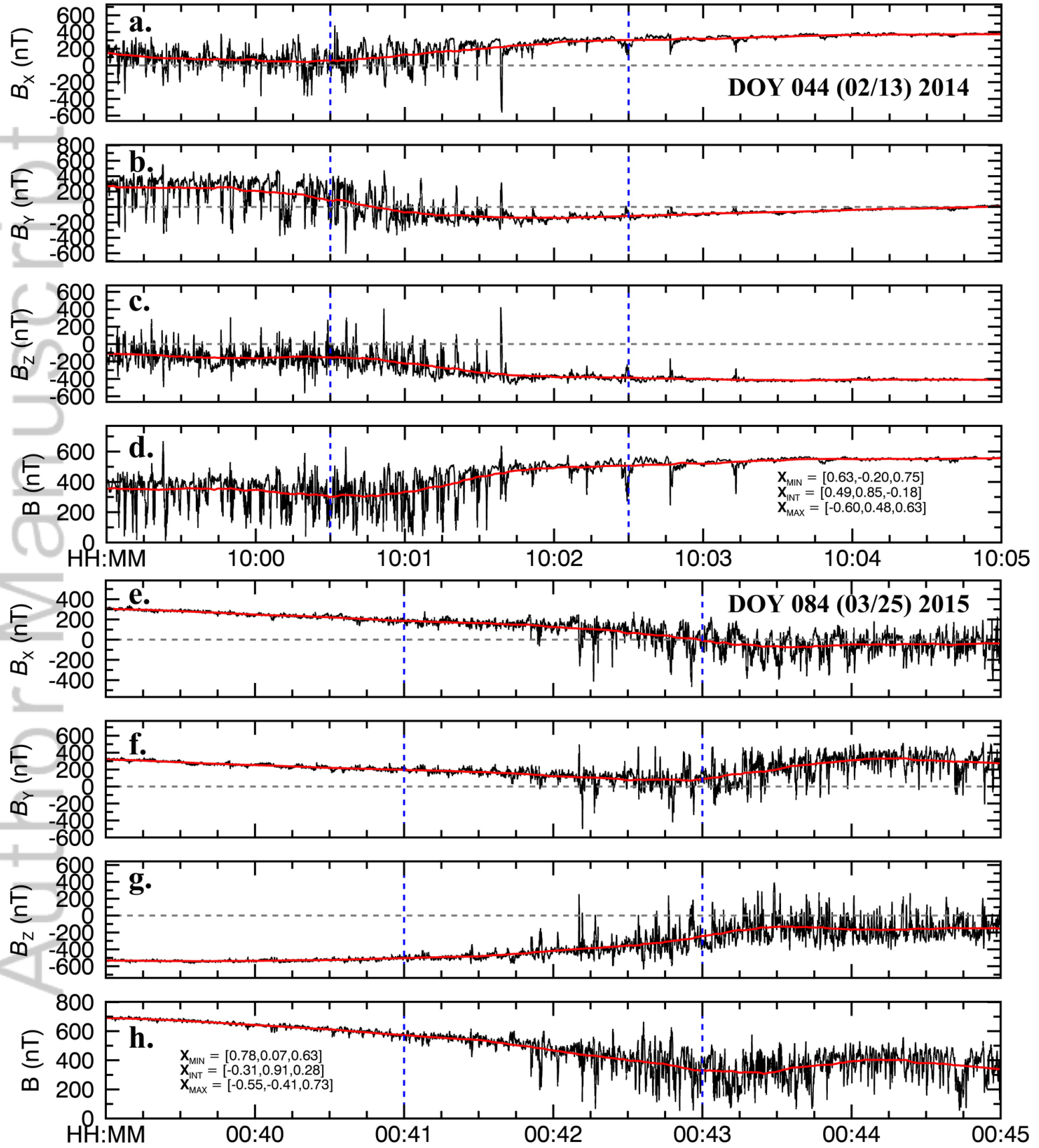2019JA026892-f08-z-.tif

2019JA026892-f09-z-.tif

2019JA026892-f10-z-.tif

MESSENGER

a.

B_X (nT)

DOY 288 (10/15) 2011

b.

B_Y (nT)

c.

B_Z (nT)

d.

B (nT)

X_{MIN} = [-0.80,-0.38,-0.46]
X_{INT} = [-0.05,0.81,-0.59]
X_{MAX} = [-0.60,0.45,0.66]

HH:MM   14:38   14:39   14:40   14:41   14:42   14:43

e.

B_X (nT)

DOY 335 (12/01) 2013

f.

B_Y (nT)

g.

B_Z (nT)

h.

B (nT)

X_{MIN} = [0.35,-0.58,0.74]
X_{INT} = [0.71,0.68,0.20]
X_{MAX} = [-0.61,0.45,0.65]

HH:MM   01:34   01:35   01:36   01:37   01:38   01:39

2019JA026892-f11-z-.jpg

MESSENGER

a.

DOY 044 (02/13) 2014

b.

c.

d.

$X_{MIN} = [0.63,-0.20,0.75]$
$X_{INT} = [0.49,0.85,-0.18]$
$X_{MAX} = [-0.60,0.48,0.63]$

e.

DOY 084 (03/25) 2015

f.

g.

h.

$X_{MIN} = [0.78,0.07,0.63]$
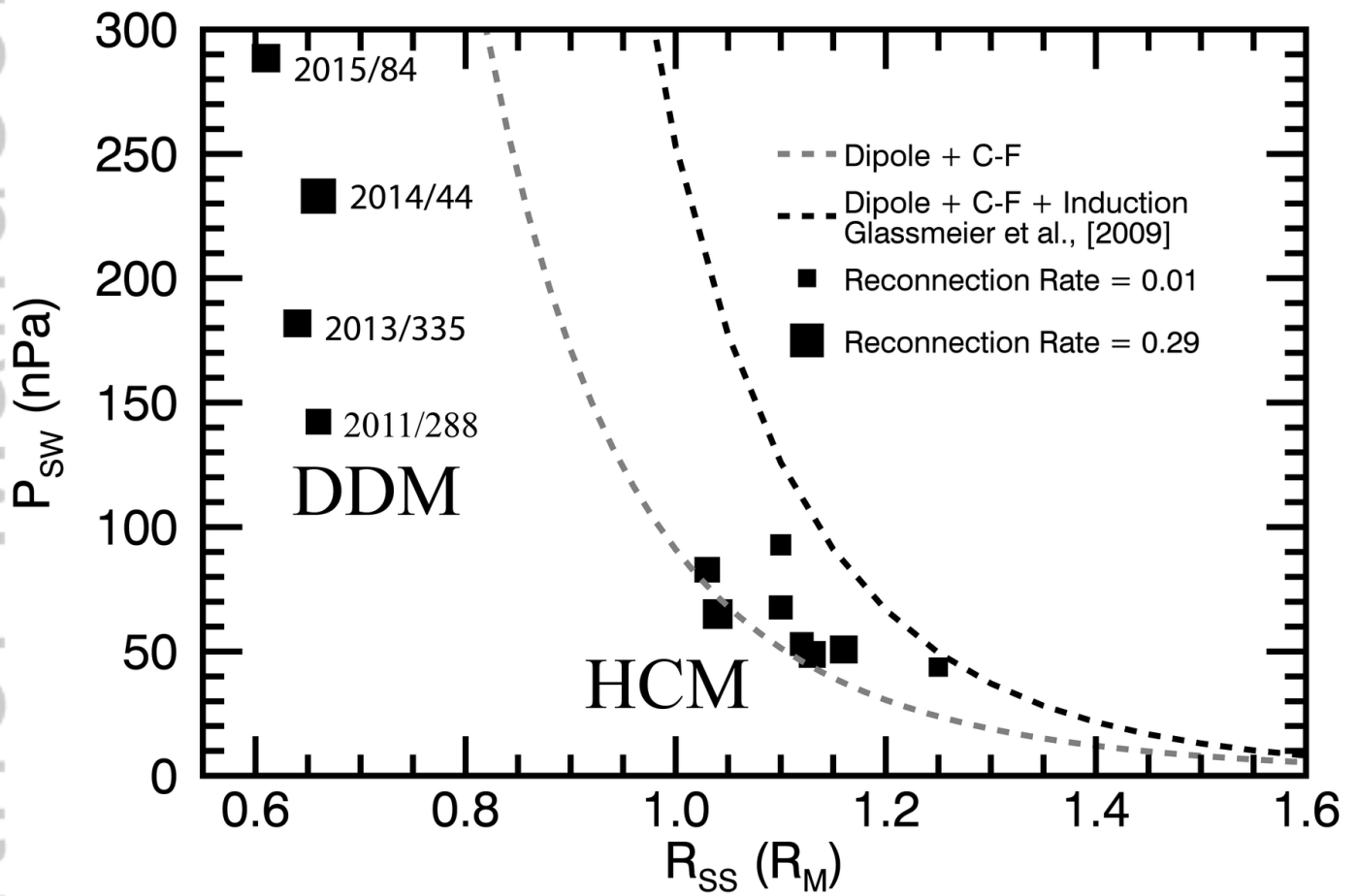$X_{INT} = [-0.31,0.91,0.28]$
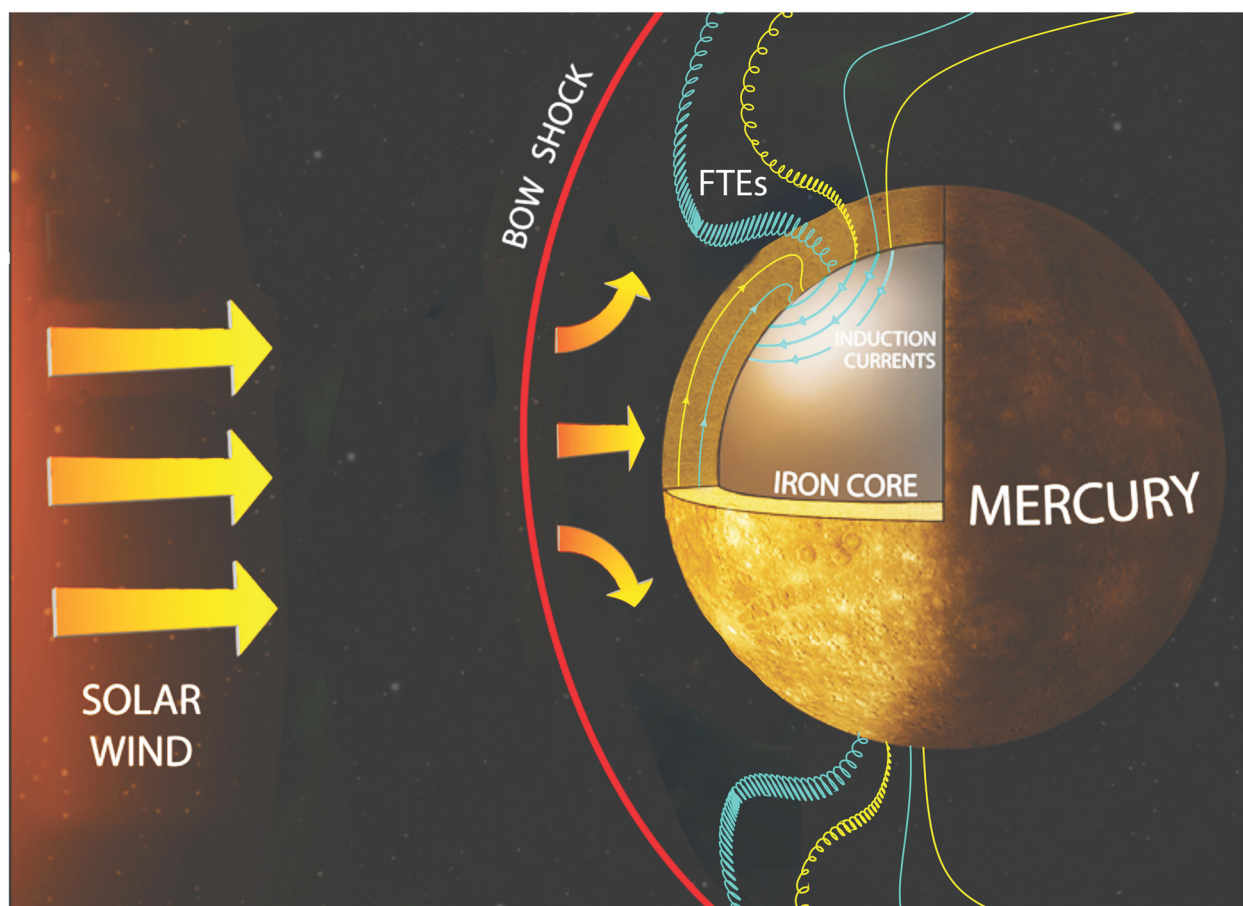$X_{MAX} = [-0.55,-0.41,0.73]$

2019JA026892-f12-z-.jpg
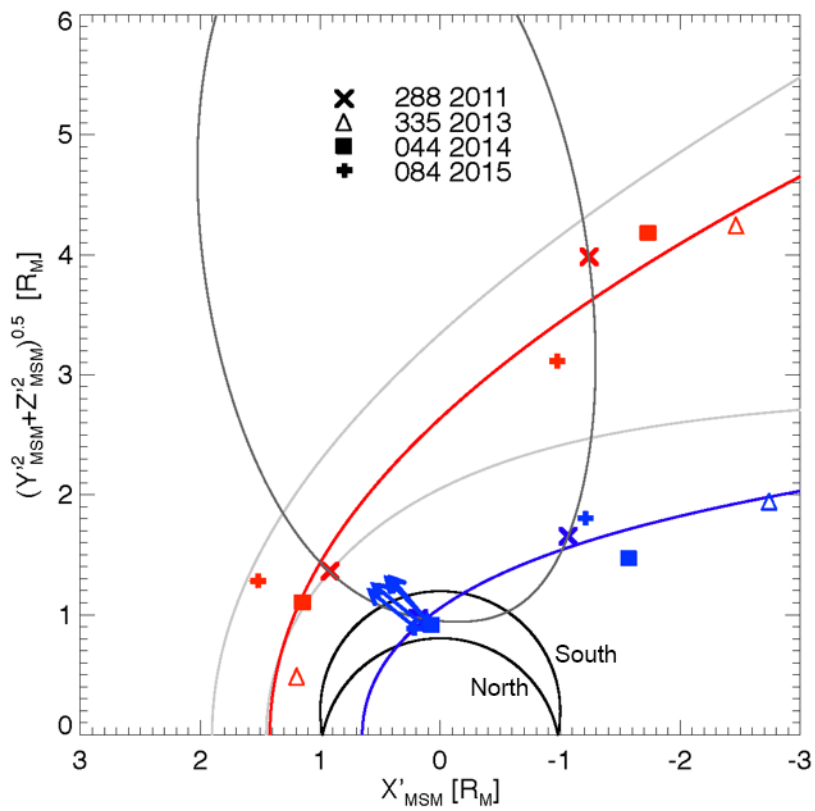
2019JA026892-f13-z-.tif

2019JA026892-f14-z-.tif

2019JA026892-f15-z-.tif